Syndeposition and epigenetic modification of the strata-bound Pb–Zn–Cu deposits associated with carbonate rocks in western Kunlun, Xinjiang, China

Zhengwei Zhang [a,*], Nengping Shen [a], Jiantang Peng [a], Xiangrong Yang [a,b], Guangyong Feng [a,b], Fu Yu [a,b], Lingjie Zhou [a,b], Yujiao Li [a,b], Chengquan Wu [a,b]

[a] State Key Laboratory of Deposit Geochemistry, Institute of Geochemistry, Chinese Academy of Sciences, 46 Guanshui Road, Guiyang 550002, China
[b] Graduate University of Chinese Academy of Sciences, Beijing 100049, China

ARTICLE INFO

ABSTRACT

Lead–zinc–copper (Pb–Zn–Cu) deposits in the western Kunlun Orogen of China are mostly distributed along the Keziletao–Kusilafu fault zones in the Palaeozoic clastic–carbonate rocks, which formed in a late Palaeozoic subsidence belt at the south-west margin of the Tarim platform. Geological and geochemical studies were conducted on these deposits including detailed field observation, petrographic study, and geochemical and isotopic analyses of sulfur, lead, strontium, rhenium–osmium, and argon isotopes, as well as fluid inclusion geochemistry. The characteristics of the deposits include: (1) Except for the Tiekelike Pb–Cu deposit associated with mid-Devonian rocks, all of the other deposits were developed in the lower layers of the early Carboniferous strata. These strata mostly comprise sedimentary dolomitic limestone, sandy limestone, black limestone, and calcareous shale. (2) The ore bodies are stratiform and host veins. The stratiform ores are coeval with host rocks (yielding ore-forming ages of 331–337 Ma), while the vein ore bodies are mostly massive deposits formed at 206–235 Ma. The isotopic compositions of the sulfur and lead reveal that the ore-forming elements originated from various sources. (3) The mineralization in cements of brecciated ore is a veinlet type, while in the breccias it is a disseminated type. The stratoid, disseminated, and framboidal structures of the ore reveal the synsedimentary ore-formation. However, the veins, mesh-veins, and massive structures indicate late stage hydrothermal mineralization. (4) The principal metallic minerals include sphalerite, galena, and pyrite, while the secondary oxide minerals include variable distributions of cerussite, anglesite and limonite. The gangue minerals include dolomite, calcite, quartz, sericite, and gypsum, with minor chert and barite. (5) The original host rocks likely experienced dolomitization, calcitization, and minor silicification. The ore deposits underwent hydrothermal alterations, sub-greenschist facies metamorphism, and brecciation. The ore deposits may have initially formed via syndeposition in a subsidence belt along the southwest margin of the late Paleozoic Tarim platform; these deposits were further modified during later hydrothermal alteration and orogenesis during the Triassic period.

© 2014 Elsevier B.V. All rights reserved.

1. Introduction

A Paleozoic clastic–carbonate formation containing strata-bound lead–zinc–copper deposits occurs along the southwest margin of the Tarim platform in the western Kunlun area of the Xinjiang Province in China (Fig. 1-a,b, Table 1). The ore deposits were associated with the Paleo-Tethys Ocean from the Devonian to the early Carboniferous Periods. The subsequent expansion and orogenesis in the region during the late-Permian to Triassic (Ji, 2005; Xiao et al., 2005) closed the Paleo-Tethys Ocean and caused extensive uplifting in the northern area of

western Kunlun (Chen et al., 2010). The tectonic event also triggered a series of orogenic hydrothermal activities and mineralization (Chen et al., 2010).

The earliest geological survey in this area was conducted in the 1940s, proposing the existence of a Pb–Zn–Cu mineralization belt (Belyaevsky, 1949). In the 1950s, a Chinese geological team (Xinjiang Metallurgy 702 Geological Brigade) performed field investigations, and more deposits were identified; the results suggested that these deposits might have had a hydrothermal origin associated with the local magmatic activities. A mineral resource map generated in the 1980s (Second Geological Brigade of the Xinjiang Geology and Mineral Bureau) suggested that these deposits contain hydrothermally altered sediment (Wang et al., 1985). Recently, many new interpretations
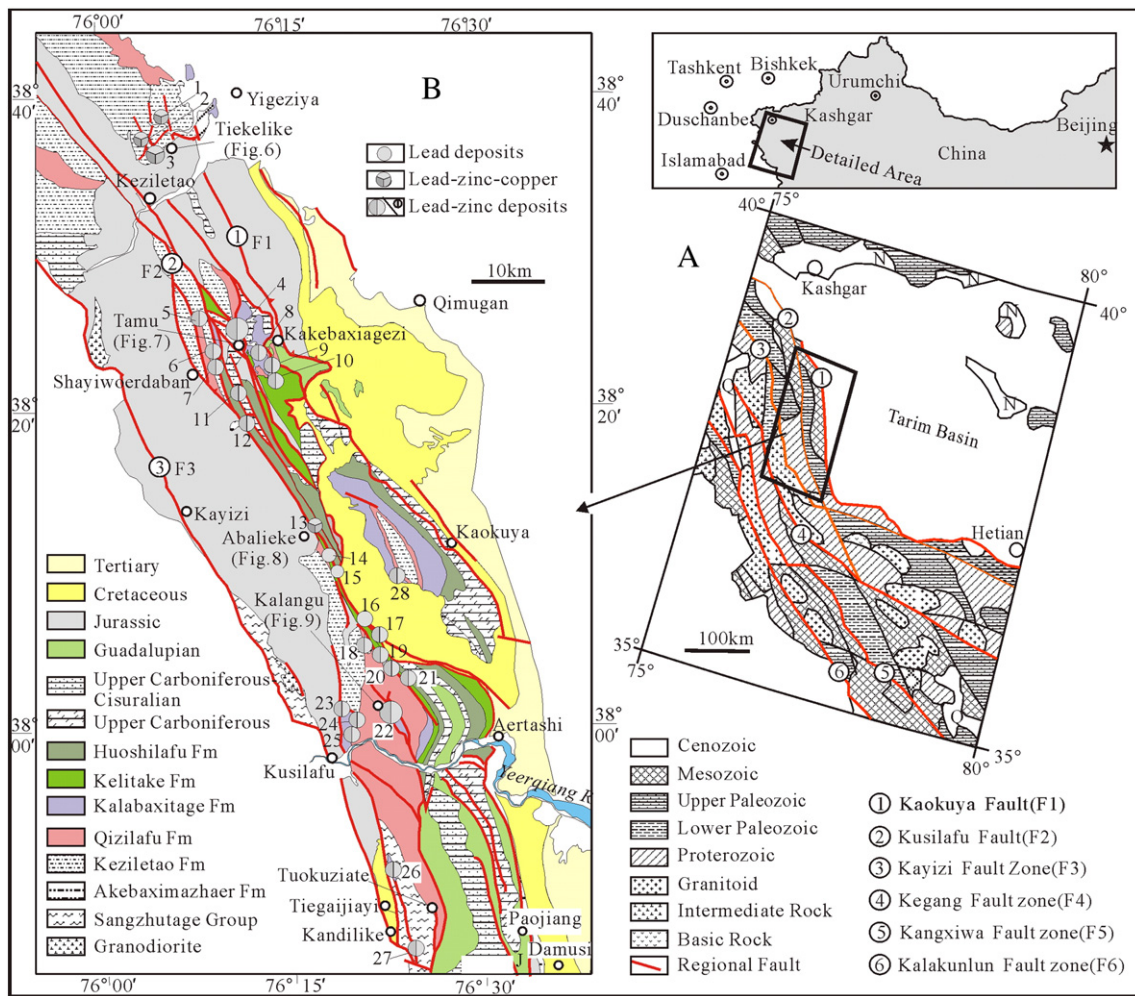
Fig. 1. Geological map showing the distribution of lead–zinc deposits in western Kunlun (modified after Henan Institute of the Geological Survey, 2006; Zhang et al., 2011a), China. Deposit numbers and local names: 1 Calabaxitage; 2 Selamujiluoke; 3 Tiekelike; 4 Tamu; 5 Shalaiyi; 6 Alaerqia; 7Sukaite; 8 the south Tamu; 9 Kaqikake; 10 Kaliyasikake, 11 Kapuka; 12 South Kapuka; 13 Abalieke; 14 Paerwan; 15 Tamuji; 16 Kezi; 17 Zuolagen; 18 North Huojilake; 19 Maridong; 20 Gemalike; 21 Adamutashi; 22 Kalangu; 23 Tuhongmulike; 24 Kalatashi; 25 Wusulike; 26 Tuokuziate; 27 Kandilike; 28 Kafuka.

regarding the origins of these diverse deposits have been proposed. Many studies have reported that most of these deposits were originally the Mississippi Valley Type (MVT) (Chang, 2003; Kuang et al., 2002; Wang et al., 2001; Zhu et al., 1998). However, different metallogenic models were suggested by different researchers, such as sedimentary exhalative deposits (Tian and Hu, 2010) and epithermal/mesothermal Pb–Zn vein deposits (Yuan, 2007).

After studying the petrological characteristics of these deposits and conducting extensive geological and geochemical analyses, this study suggests that the ore-bearing host rocks might have been initially deposited during the late Paleozoic period; subsequently, these deposits were subjected to syn-depositional mineralization along the platform margin of the subsiding basin associated with the initial Paleo-Tethys expansion. During the subsequent Paleo-Tethys ocean closure from the late-Permian to the Triassic, additional hydrothermal fluid overprinted on the strata-bound Pb–Zn–Cu deposits hosted by clastic carbonate (Zhang et al., 2011a). This complex history might explain the multiple-origin characteristics exhibited by many of these deposits.

2. Regional geology and tectonic evolution

2.1. Tectonic setting

The geological evolution of the western Kunlun area is related to the southwestern Paleo-continental margin of the Tarim platform (Mattem

et al., 1996). Three tectonic events were critical to the evolution of the western Kunlun orogenic belt in Xinjiang (Bi et al, 1999; Cheng and Xu, 2001; Cheng and Zhang, 2000; Cheng et al., 1993; Cui et al., 2006; Liu, 2001; Pan, 1990; Yang, 1994) (Fig. 1-A).

Beginning in the Ediacaran period, the southern margin of the Tarim platform expanded to form the Proto-Tethys Ocean (Jiang et al., 1992). By Late Paleozoic, the Proto-Tethys Ocean expanded further to form the Paleo-Tethyan Ocean (Li and Yin, 2002; Pan et al., 2000; Xiao et al., 2005). During this period, multiple mineralization events occurred in this region (Hou et al., 2007; Li et al., 2007; Qi et al., 2005; Sun et al., 2003; Wang and Wu, 1997; Wang et al., 2008). The crust extended from Late Devonian to Early Carboniferous, forming the Paleo-Tethys Ocean along the current southern Kangxiwa fault (Wang et al., 2006) and generating the Aoyitag–Kuerliang continental rift sedimentation in the southwestern margin of the Tarim Basin (Fig. 1-A). The crust extension enabled the formation of volcanogenic polymetallic sulfide deposits (Jia et al., 1999). From Carboniferous to Early Permian, clastic–carbonate rocks were deposited in the continental basin (Fig. 1-B) overlying on the Devonian formations (Zhang et al., 2009). By the end of Carboniferous (300 Ma), the Paleo-Tethys Ocean began to close in the north, diminishing in size during Triassic along the current Kangxiwa fault (F5 in Fig. 1-A). These orogenic events generated a large thrust zone, forming low greenschist in the Permian–Triassic rocks (Liu et al., 2003) from south to north (F1 and F2 in Fig. 1-B). From Late Triassic to Cretaceous, a Jurassic foreland compressional basin developed along the

Table 1
Characteristics of Pb–Zn–Cu strata-bound deposits in carbonates in the western Kunlun.

Deposit no. longitude, latitude location	Deposit type and metallogenic epoch (method/mineral/age)	Ore-forming element association reserve (Pb–Zn–Cu metal)	Ore body morphology and position within host rocks	Mineral association within ore body	Ore structure and texture and the grade of metal	Host rock and altered wall rock	Ore-controlling structures and the other deposits
No. 1 Tiekelike 76°04′00″, 38°37′00″ Akto County	Synsedimentary-succeeding transformation (Re–Os isotopic dating/chalcopyrite/226 Ma)[a]	Cu–Pb (Zn. Ag) Medium (120,300 t)	Disseminated chalcopyrite within the quartz sandstone, within bedded ore body. Length 2000 m, width 70–220 m. Multilayer galena occurrence to the carbonate, with quasi-lamellar or bedded shape in the breccia zone. Part galena and chalcopyrite occurrence with nervation. Maximum thickness 3 m, minimum thickness 1 m, ore body average thickness 2 m, length 200 m	Mainly galena, chalcopyrite and pyrite with minor chalcocite. Secondary azurite, malachite, cerussite and jarosite. Gangue minerals: quartz and calcite	Idiomorphic granular, replacement and poikilitic texture. Mainly colloform structure, with minor crumpled structure, brecciated and disseminated structure. Lead grade of metal within 0.7%–2.78%, zinc grade lower, associated with silver than cut-off grade (50 g/t)	Middle Devonian Keziletao F., Upper Devonian Qizilafu F., Lower Carboniferous Kalabaxitage F.; Ore body within tawny phyllite and quartzite in Middle Devonian Keziletao F.; Altered wall rock: mainly dolomitization and calcitization, with minor silicification	North-east strike fault cutting inclined fold, contemporaneous fault occurrence with tectonic breccia. Other deposits: Kalabaxitage (No. l) and Selamujiluoke (No. 2) lead–zinc deposits
No. 2 Tamu 76°11′08″, 38°25′27″ Akto County	Synsedimentary-succeeding transformation (Re–Os isotopic dating/chalcopyrite/337 Ma)[b] (Ar–Ar isotopic dating/quartz/235 Ma)[c]	Zn (Pb, Co) Large (893,l00 t)	Mineralized and breccia zone with same occurrence to the stratum, length 800 m, maximum thickness 40 m. width 30–70 m. Multilayer ore body occurrence with quasi-lamellar or bedded shape in the breccia zone. Single extending vertical 500 m, greater than length 100 m, occurrence with quasi-lamellar, nervation or stockwork within the dolomitite and dolomitic limestone.	Mainly blende, with minor galena and pyrite. Secondary cerussite, sardinianite and ferrimanganic oxide. Gangue minerals: dolomite, calcite, quartz and muscovite	Framboidal, exsolution and metasomatic relict texture. Banded, flow, brecciated, veiny and disseminated structure. Zinc grade of metal within 1.28%–9.25%, lead grade lower, associated with silver than cut-off grade (50 g/t)	Ore body within thick-layer dolomitite and dolomitic limestone in Lower Carboniferous Kalabaxitage F.; Altered wall rock: mainly dolomitization, silicification and pyritization with minor chloritization	North-east strike fault cutting overturned fold, contemporaneous fault occurrence with tectonic breccia. Other deposits: Alaerqia (No. 6), Kaqikake (No. 9) and Kaliyasikake (No. 10) lead–zinc deposit
No. 3 Abalieke 76°22′00″, 38°10′00″ Akto County	Synsedimentary-succeeding transformation (Re–Os isotopic dating/chalcopyrite and pyrite/331 Ma)[d]	Cu–Pb (Zn–Ag) Medium (103,300 t)	Multilayer occurrence with lenticular ore body within dolomitite side in the contact zones of quartz sandstone and dolomitite, length 300 m, maximum thickness 20 m, extending vertical 400 m	Mainly chalcopyrite, galena and pyrite with minor blende. Gangue minerals: dolomite, calcite, quartz and muscovite	Framboidal, grating, idiomorphic granular texture, crush and replacement texture, with massive and disseminated structure. Lead grade of metal within 0.70%–6.54%, zinc grade lower <0.3%, copper grade of metal within 0.6%–3.5%	Ore body within dolomitite in Lower Carboniferous Huoshilafu F.; Altered wall rock: mainly dolomitization, silicification and pyritization with minor chloritization	North-west strike fault cutting upright fold with tectonic breccia. Other deposits: Paerwan (No. 14) and Tamuji (No. 15) lead–zinc deposit
No. 4 Kalangu 76°23′12″, 38°01′20″ Akto County	Synsedimentary-succeeding transformation (Ar–Ar isotopic dating/blende/235 Ma)[e]	Pb (Zn–Co) Large (630,300 t)	Mineralized and breccia zone within dolomitic limestone, length 500 m, maximum thickness 30 m, width 30–60 m. Multilayer occurrence with lenticular or quasi-lamellar shape within dolomitic limestone side in the contact zones with quartz gravel carbonate	Mainly galena with minor chalcopyrite, pyrite, blende and chloanthite. Secondary malachite, covellite, chalcocite, erythrite, cerussite and ferrimanganic oxide. Gangue minerals: dolomite and calcite	Granular, coarse-grained, skeletal and replacement texture, with disseminated and vein structure. Lead ore grades from 0.80% to 8.90%, zinc grade lower <0.30%, associated with cobalt than cut-off grade (0.02%)	Ore body within limestone, carbonaceous limestone and dolomitic limestone in the Lower Carboniferous Kalabaxitage F.; Altered wall rock: mainly dolomitization and silicification	North-west strike fault cutting disharmonic fold, drag fold occurrence with tectonic breccia. Other deposits: Tuohongmulike (No. 23), Kalatashi (No. 24) and Wusulike (No. 25) deposit
No. 5 Tuokuziate 76°23′05″′–03″′, 37°50′27″–16″ Shache County	Synsedimentary-succeeding transformation (Syngenetic sedimentation and epigenetic reform)	Pb–Zu (Ag) Small (31,100 t)	Mineralized zone length 500 m. Multilayer ore body occurrence with lenticular, quasi–lamellar or bedded shape within dolomitic limestone side in the contact zones of dolomitic limestone and carbonaceous limestone	Mainly galena and blende with minor pyrite. Gangue minerals: quartz and calcite	Cementation, radial and mid-fine-grained texture. Mainly massive, stripped and brecciated structure with minor disseminated structure. Ore analysis results: Pb 33.13%, Zn 21.80%, Ag 169 g/t	Ore body within limestone, carbonaceous limestone and dolomitic limestone in the Lower Carboniferous Kalabaxitage F.; Altered wall rock: weakly silicification and dolomitization	North-east strike fault cutting north-west strike fold, occurrence with tectonic breccia. Other deposits: Kandilike (No. 27) lead–zinc deposit

The ore deposit characteristics are compiled based on Zhang et al. (2009; 2011a).
In the table "Deposit No." is the same as Fig. 1. "[a, c, e]" from Zhang et al. (2011a). "[b]" from Yang (2009). "[d]" from Zhang et al. (2011b).

	Formation	Stratigraphic column	Thickness (m)	Lithological description
Permian Upper	Daliyueer		694	Clastic rocks with fine-grain quartz sandstone, quartz siltstone and argillaceous shale, interbedded with two layer impure limestone containing silty micrite
Middle	Qipan		485	Shallow-marine carbonate and clastic rocks, the former containing limestones and sparite limestones, the latter clastic rock comprising quartz, feldspar, etc
Lower	Keziliqiman		190	Black grey bedded micrite, bioclastic silty limestone, oolitic limestone and micrite
Carboniferous Upper	Tahaqi		281	Shallow marine facies carbonate interbedded with clastic rock, bioclastic limestone, micrite
Upper	Azigan		337	Carbonate interbedded with clastic rock, crystalline limestone, calcareous sandstone etc
	Kalawuyi		320	Mainly limestone, bioclastic limestone, lithic quartz sandstone, calcareous siltstone, etc
Lower	Huoshilafu (Ledge)		732	A fossil-rich carbonate platform interbedded with clastic rock, lowerpart mainly grey black thin-bedded siltstone, argillaceous limestone interbedded with brown quartz packsand, thin-bedded feldspar quartz sandstone etc; upperpart mainly dark grey middle-thick-bedded limestone, micrite
Kelitake	Kelitage		725	Littoral facies single carbonate sedimentary environment, rock assemblage consist of mainly mid to thick-bedded limestone, bioclastic limestone, oolitic limestone, dolomite, dolomitic limestone etc
	Kalabaxitage (Ledge)			
Devonian Upper	Qizilafu		653	Coastal - continental facies deposition, rock assemblage consist of mainly purple red quartz sandstone, siltstone interbedded with thin conglomerate partly
Middle	Keziletao (Ledge)		1737	Coastal - continental facies calcareous thin clastic rock interbedded with minor carbonate deposition, rock assemblage consist of mainly calcareous sandstone, siltstone, mudstone, bioclastic limestone etc.
	Akebaxizhayier		1151	Epizonal metamorphic terrigenous clastic rock, rock assemblage consist of mainly quartz sandstone, siltstone, quartz conglomerate, quartz gritstone and minor silt mudstone
Precambrian	Sangzhutage group			Greenschist facies—low amphibolite facies metamorphic rock, lower part mainly banded-ocular migmatite interbedded with sericite quartz; and upperpart mainly sericite chlorite quartz schist, garnet plagioclase schist as well as granulite and gneiss.

Ledge: ore-bearing layer

Fig. 2. Stratigraphic column of the host rocks for the lead–zinc deposits in western Kunlun (modified after Henan Institute of the Geological Survey, 2006; Zhang et al., 2011a).

northern edge of the Tarim Basin. Meanwhile, numerous internal Jurassic coal basins also developed in the southern margin of the Tarim Basin.

From Late Cretaceous to Eocene, the Neo-Tethys Ocean drifted northward along the current Brahmaputra River to form the Kalakorum fold (Cheng et al., 1993). Along the southwestern margin of the Tarim Basin, a large piece of crust collided with the inland basin (Qu et al., 2004), forming a ductile shear zone with a thrust-nappe structure from south to north (Xinjiang Geological and Mineral Bureau, 2003). After the Neo-Tethys Ocean closed during the Eocene, the continuing subduction of the Indian Plate under the Eurasia Plate generated numerous strike-slip faults nearby (Henan Institute of the Geological Survey, 2006).

2.2. Host rocks

The ore-hosting rocks include Precambrian to Cenozoic strata (Xinjiang Geological and Mineral Bureau, 2003). The Precambrian basement consists of Paleoproterozoic metamorphic rocks from the Heluositan and Sailajiazige Formations, and their protoliths are igneous and sedimentary rocks. The basement is covered by Paleozoic epimetamorphic sediments from the Jixianian Formation.

The Devonian, Carboniferous, and Permian rocks were deposited above the basement during the Paleozoic Era. A description of these rocks is provided in Fig. 2. The Paleozoic sediments are host rocks for the Pb–Zn ore beds. The Triassic strata are absent in this area. The
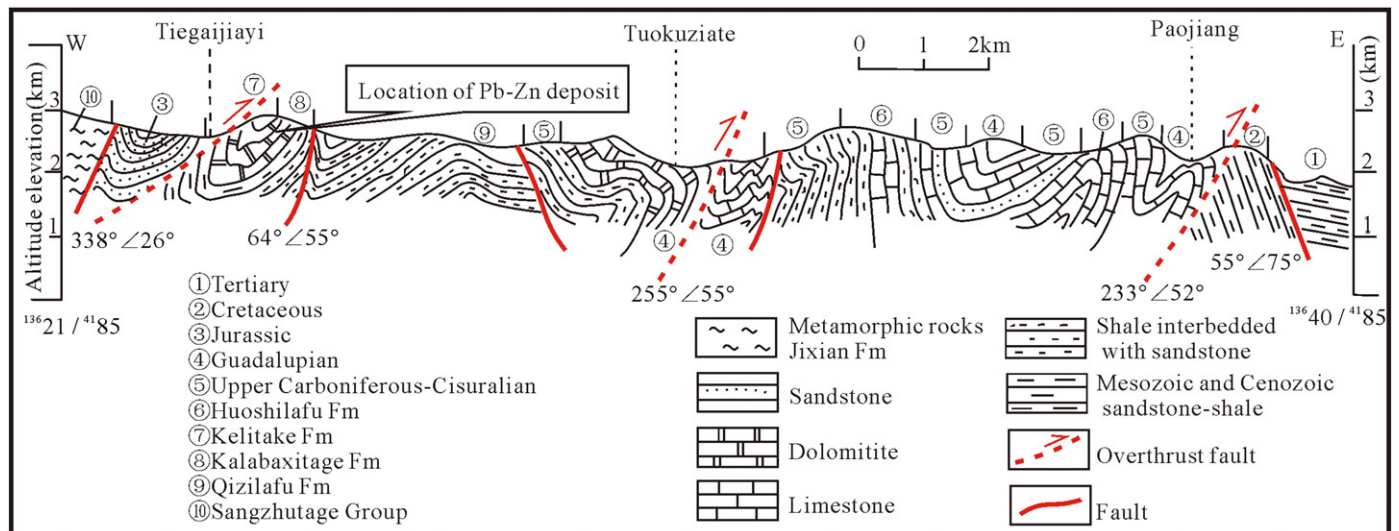

①Tertiary
②Cretaceous
③Jurassic
④Guadalupian
⑤Upper Carboniferous-Cisuralian
⑥Huoshilafu Fm
⑦Kelitake Fm
⑧Kalabaxitage Fm
⑨Qizilafu Fm
⑩Sangzhutage Group

Fig. 3. Geological cross section from Tegaijayi to Paojiang based on field measurements taken in 2008, Institute of Geochemistry, Chinese Academy of Sciences. The stratigraphic unit symbols are shown in Fig. 1.
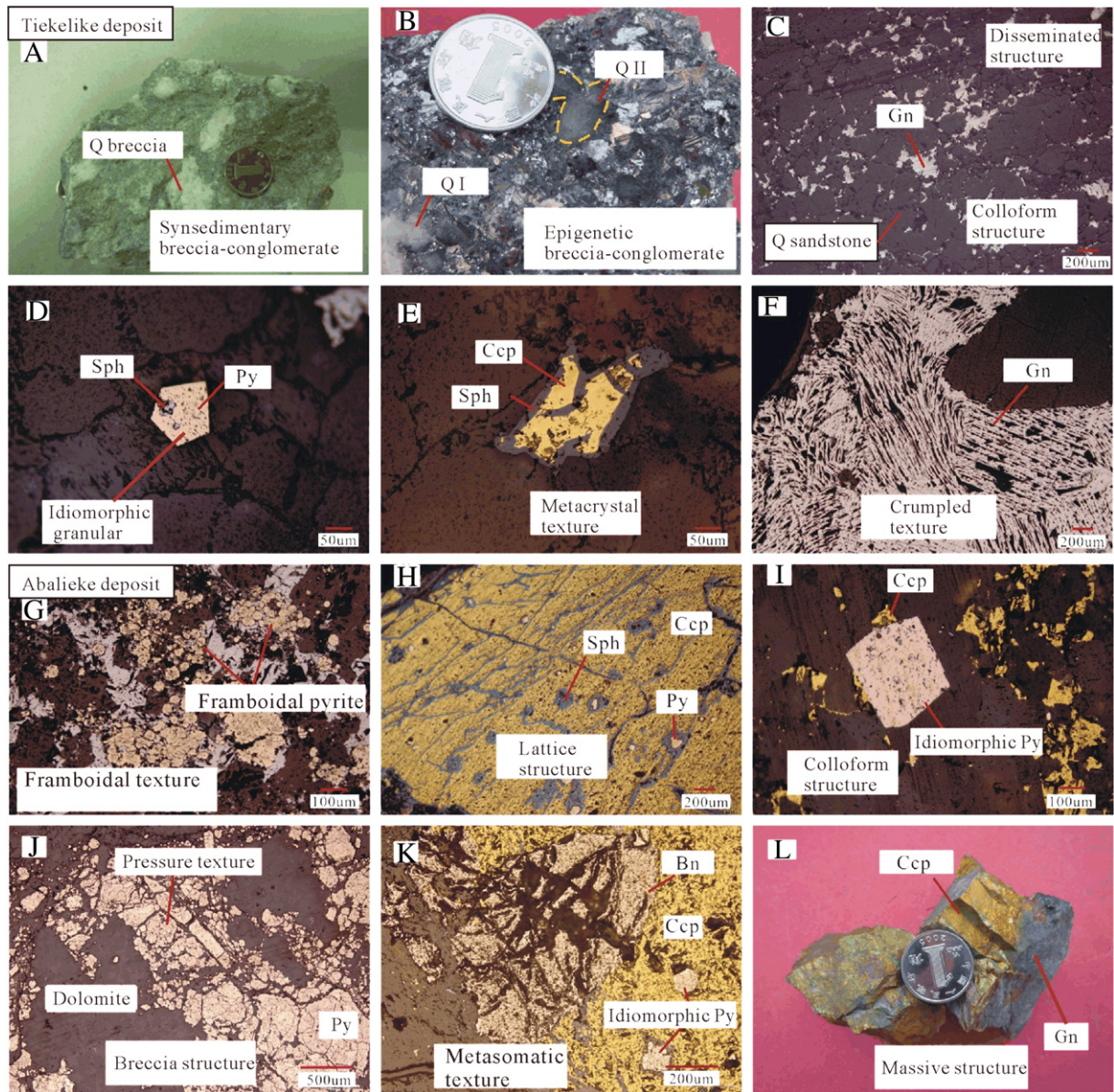
Fig. 4. Photos of the ore textures and structures from the Tiekelike (A–F) and Abalieke (G–L) deposits. A: Synsedimentary breccia–conglomerate: Mainly oval quartz with particle sizes of 0.3–0.8 cm. B: Epigenetic breccia–conglomerate: Carbonate breccia, galena, and irregular quartz breccia with endolithic brecciation. C: Galena in sandstone showing a cemented texture and a disseminated granular structure. D: Metacrystalline texture with pyrite, replaced by sphalerite. E: Metasomatic texture with chalcopyrite replaced by sphalerite along the edge. F: Crumpled galena structure. G: Framboidal texture: framboidal pyrite within carbonate. H: Grating structure composed of chalcopyrite and sphalerite with pyrite within the chalcopyrite and sphalerite, where pyrite primarily exhibits a hypidiomorphic–allotriomorphic crystal granular texture. I: Metacrystalline texture with chalcopyrite replaced by pyrite where the chalcopyrite in the fissures had a colloform structure. J: Pressure texture: pyrite crushed under stress within dolomite shows a breccia structure. K: Bornite replaced by chalcopyrite, showing the metasomatic texture. L: Chalcopyrite and galena ore showing a massive structure.

Jurassic rock consists of coal-rich fluvial sediments. The Cretaceous strata consist of lagoonal and neritic red clastic rock intercalated with sedimentary carbonate. The Tertiary rocks are gypsum and carbonate deposits, while the Quaternary sediment consists of intermountain clastic deposits (Xinjiang Geological and Mineral Bureau, 2003).

2.3. Structure

Several major fault belts occur in this region. The Kaokuya fault belt (F1 in Fig. 1-B) is located in the Yigeziya–Kaokuya region and strikes 320°. The central area of this belt exhibits a curved bend where the topography changes to a SW strike of 220° and a steep dip angle (44°), as shown in Fig. 1.

The Kusilafu–Keziletao fault belt (F2 in Fig. 1-B) is located in the Keziletao–Kusilafu region. Cataclasites are visible on both sides of the fault zone and are especially abundant on the eastern side of the foot-wall. This fault belt shows compressional characteristics, as suggested by the presence of schist, mylonite, and cataclasite.

The Kusilafu–Keziletao fault belt might have formed in the Variscan orogeny, while the Kaokuya fault belt might be dated at least to the Cenozoic period (Henan Institute of the Geological Survey, 2006). Several of thrust faults and closed folds were observed between the Kaokuya fault and the Kusilafu fault (Fig. 1-B). Numerous traction folds are developed on both sides of the Kusilafu fault. These folds are mostly inclined with south to southwest dip, but closed or supine folds also occur in some regions. A thrust-nappe structure with a south-west to northeast orientation is apparent in the region (Fig. 3).
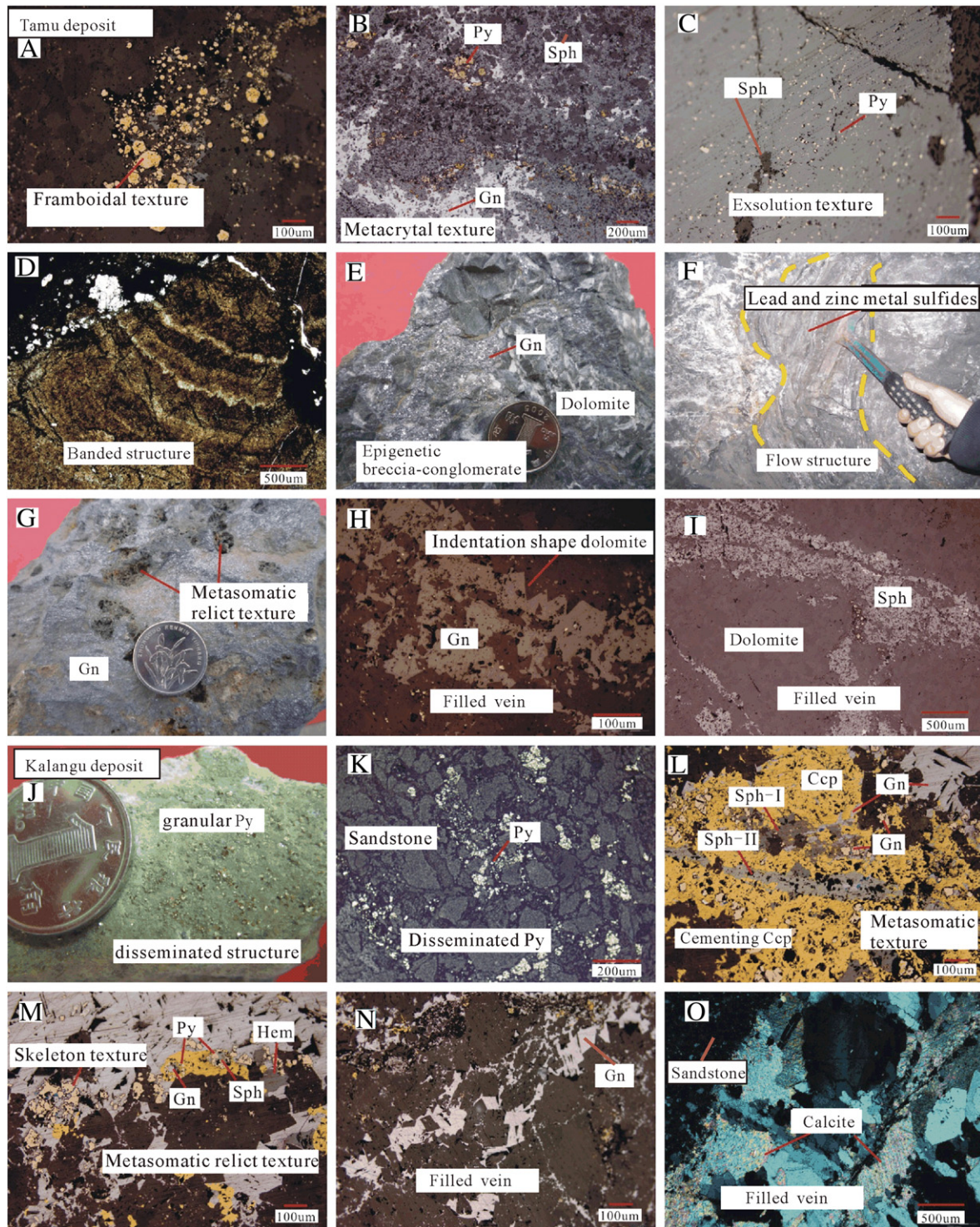
Fig. 5. Photographs of the ore structures from the Tamu deposit (A–I) and the Kalangu lead deposit (J–O). A: Framboidal pyrite. B: Early pyrite and galena replaced by sphalerite. C: Sphalerite and pyrite showing an exsolution texture, idiomorphic crystal grains, and a lamellar texture. D: Dolomite or calcite with tint sphalerite in ore with a banded structure. E: Galena filling a fissure within the fracture zone due to the endolithic pressure stress. F: Flow structure: metal sulfide filled fissures due to the endolithic pressure stress, with folding. G: Corroded galena showing metasomatic relict texture. H: Galena veins with indentations or angular shapes in dolomite. I: Sphalerite veins in dolomite with completely filled fissures. J: Pyrite showing a disseminated granular structure. K: Disseminated pyrite within sandstone. L: Early stage allotriomorphic crystalline pyrite replaced by sphalerite and chalcopyrite; phase I sphalerite (Sph-I) replaced by chalcopyrite and showing a cemented texture; Sph-I and chalcopyrite penetrated by galena within fissures; chalcopyrite penetrated by the latest sphalerite (Sph-II) as veins showing a penetrative texture. M: Pyrite replaced by galena showing a skeletal texture; chalcopyrite replaced by sphalerite with pyrite and galena showing a metasomatic relict texture. N: Galena in dolomite occurring as nervation with indentations or angular shapes. O: Calcite veins in sandstone.

3. Deposit description

The metallogenic belt is located between the Kaokuya fault belt (F1 in Fig. 1-B) and the Keziletao–Kusilafu fault belt (F2 in Fig. 1-B). This area is part of the Qiaerlong–Kuerliang Carboniferous continental back–arc extensional subsiding basin or the late Paleozoic subsiding basin in the southwestern margin of the Tarim platform. The subsiding basin is located on the inner edge of the Proterozoic Tiekelike uplift
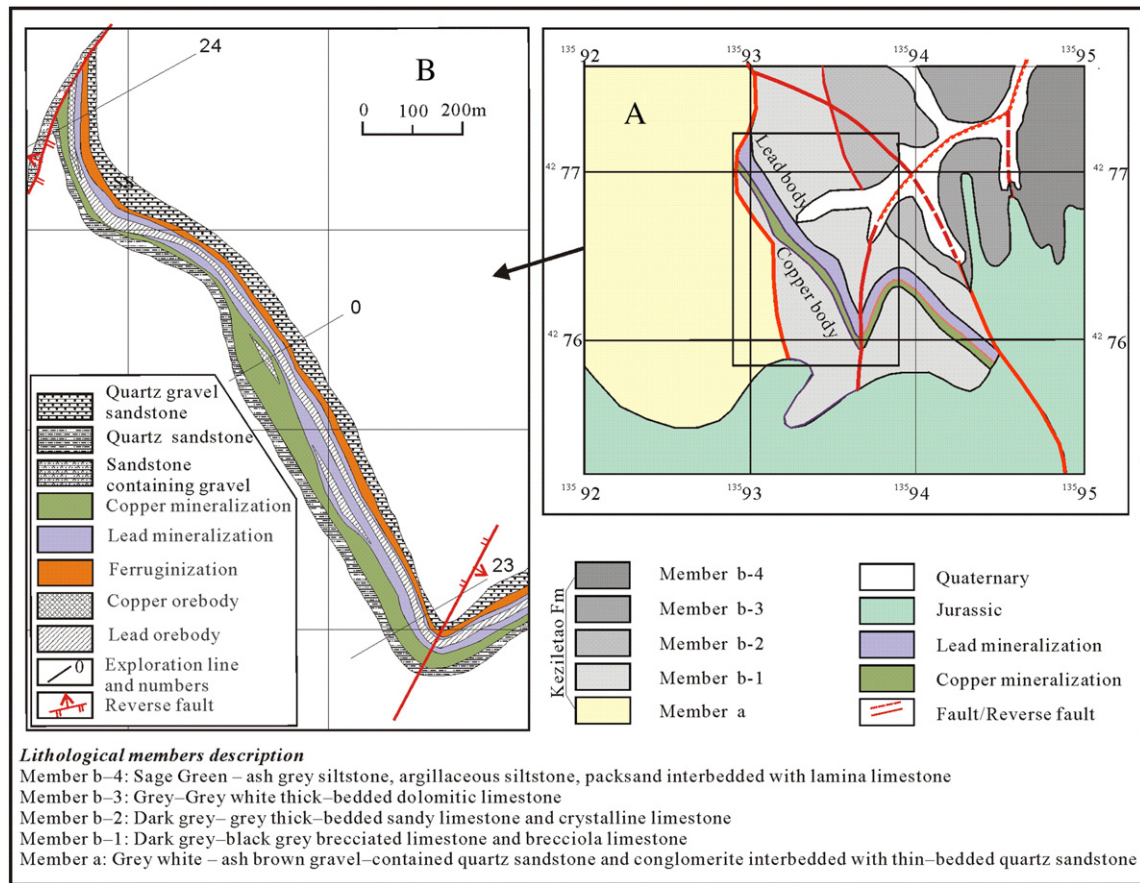
Fig. 6. Geological map of copper–lead deposits (A) and a sketch showing the ore body zonation (B) in Tiekelike deposits (edited after Zhang et al., 2011a).

(Fig. 1-A) (Dong et al., 2007). No magmatic activity was observed in this area except for some minor dolerite dykes.

In the study area, 28 known deposits (Fig. 1-b, Table 1), including Tiekelike, Tamu, Abalieke, and Kalangu, are observed from north to south (You et al., 2012). These ore bodies occur as either stratiform horizons within the host rock or veins within the fault zones. The stratiform ore bodies are mostly confined to host rocks that show typical sedimentary characteristics (Fig. 4 A, E; Fig. 5 A, D). The ore bodies associated with the veins have high-grade mineralization and characteristics of late filling and replacement (Fig. 4 B, I, J; Fig. 5 B, M, N) after mineralization.

3.1. Tiekelike lead–copper deposit

The Tiekelike lead–copper deposit is located near the Keziletao Township of Akto County (Fig. 1-B, Table 1). The stratigraphy and lithology of the area are shown in Figs. 1 and 2, respectively. The exposed strata are parts of the mid-Devonian Akebaximazhaer, Keziletao and lower Jurassic Shalitashi Formation. The strike of the rock units in strata is usually toward the NNW, dipping to the NE. Some layers have a SW dip due to faulting (Fig. 6).

The mid-Devonian Keziletao Formation is the ore-bearing layer and can be further divided into four lithological units (Fig. 6A). The mineralization occurs primarily in the medium-grained calcareous cemented quartz sandstone in the middle of the first unit and appears stratiform or stratoid; this behavior is largely restricted to the formation. Some individual fault zones may intersect with different rock layers (Fig. 6 B). The mineralization zone is approximately 50 m thick and 1450 m long and contains two ore bodies: the upper layer contains lead and the lower layer contains copper. The upper layer is approximately 1000 m

long, averages 8 m thick, and contains 3% lead on average, whereas the copper mineralization is inhomogeneous in the lower layer.

The major minerals in this deposit include galena, chalcopyrite, pyrite, and chalcocite. The secondary minerals include azurite, malachite, cerussite and jarosite. The gangue minerals are mainly quartz and calcite.

The ore bodies have a crystalline texture and are dominated by breccias or disseminated mineralization. Among the brecciated rocks, the syngeneic breccias (Fig. 4-A) are oval or irregular; they have a particle size of 0.3–0.8 cm and originate from the fractured accumulation of quartz during mineralization. The epigenetic breccias (Fig. 4-B) can be further classified based on the quartz development. The type I breccias are mainly smooth and oval-spherical quartz in shape, and the type II breccias are usually milky quartz and have prominent fractures. The cementation texture (Fig. 4-C) contains mainly fine, magenta sandstone grains. The euhedral texture contains pentagonal crystalline pyrite surrounded by dark hosting rocks (Fig. 4-D). The metasomatic texture (Fig. 4-E) contains mostly sphalerite replacing chalcopyrite along the edge. The crumpled texture reflects the structural deformation of the minerals during the late stages of mineralization (Fig. 4-F).

The deposit has been subjected to hydrothermal alterations, such as silicification, calcitization, and sericitization. Silicification is the most common process and is closely related to the modification of galena ore bodies. Although the ore deposits are mainly disseminated, localized ore-veins with coarse-grained galena are observed locally.

3.2. Tamu zinc–lead deposit

The Tamu zinc–lead deposits are located near the Keziletao Township of Akto County (Fig. 1-B, Table 1). The hosting rocks belong to the
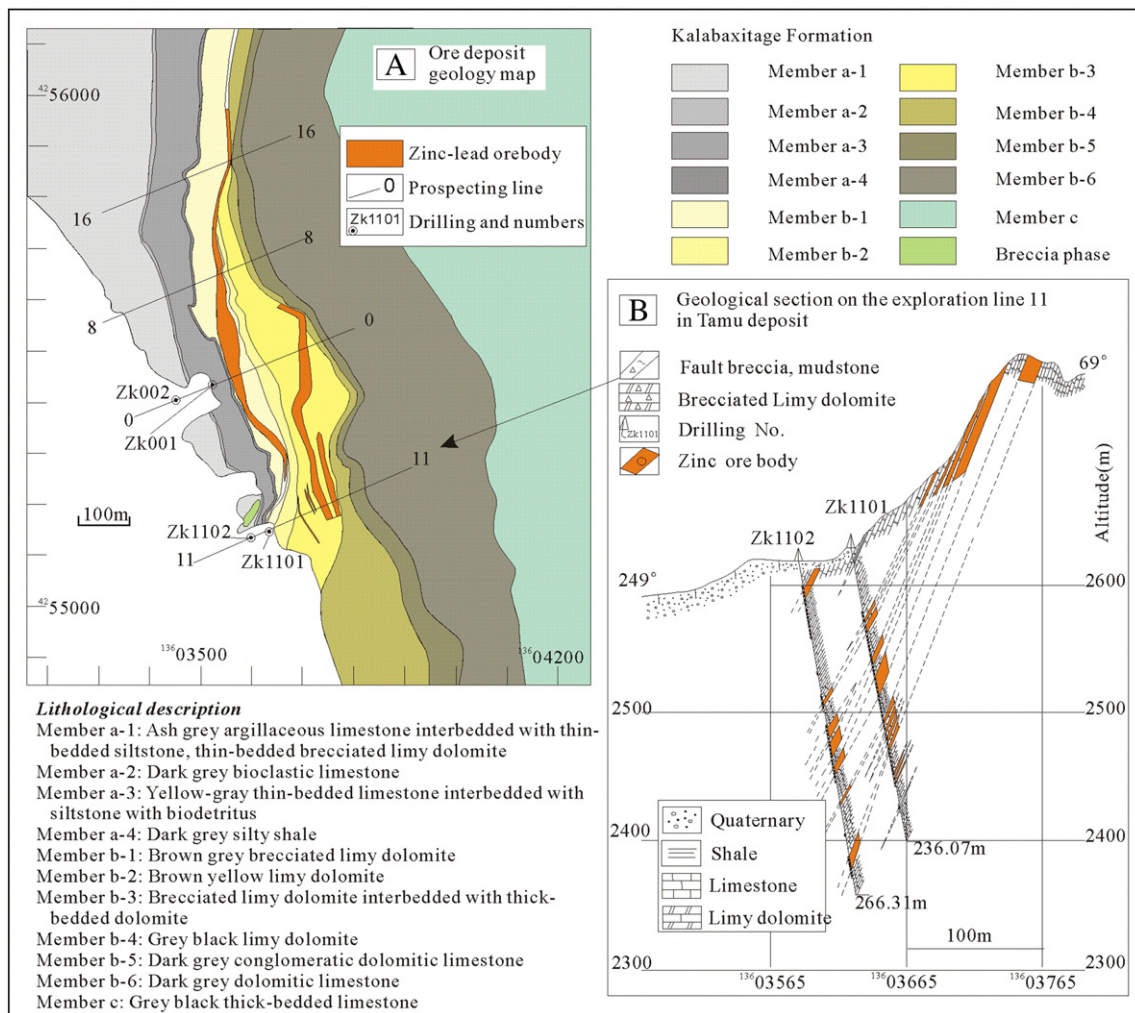
Fig. 7. Geological map of zinc–lead deposits (A) and cross-sectional map of the No. 11 prospecting line (B) in Tamu (edited after Zhang et al., 2011a).

lower Carboniferous Kalabaxitage Formation; this formation can be divided into three members consisting of 11 beds (Fig. 7 A). The ore bodies are hosted in the thick-layered dolomite and the dolomitic limestone of the lower member (Member a), as well as in the brecciated dolomite of the higher member (Member b). The breccias are typically 2 to 5 cm in diameter. The NNW breccia zone exceeds 1500 m in length. The lower ore layer is located in the fault zone adjacent to the gray calcareous sandstone and siltstone.

Mineralization occurs within the breccia zones and has the same orientation as the hosting formation. The mineralization zone is 800 m long, up to 40 m thick, and consists of multiple ore bodies. The ore bodies are mostly stratoid (Fig. 7 B). The ore bodies have a complex occurrence within the breccia zone, where numerous irregular nest-like bodies are observed with an intermittent length exceeding 300 m. The ore body approaches 30 m in width.

The major ore minerals in this deposit include sphalerite, galena, and pyrite, while the secondary minerals include cerussite, anglesite, and limonite. Sphalerite has multi-phase metallogenic characteristics and includes at least four colors, ranging from black to light yellow; these colors are indicative of temporal evolution. The hosting minerals include dolomite, calcite, quartz, and muscovite. These mineralizations are divided into two stages. Dense zinc-rich ores were formed during the first stage, while lead-rich vein ores were formed during the second stage. The ores of the veined type are coarser and contain both lead and zinc. In addition, feldspars have been found in the Tamu lead–zinc deposit during microscopic identification and electron probe analysis

(Yang, 2009). The feldspars are mostly granular (0.01–0.1 mm) and zonal.

The ores are associated with framboidal, banded, brecciated, and filled veins (Fig. 5). The majority of the pyrite is framboidal and is distributed among the carbonate fractures that formed during the early stage (Fig. 5-A). Some pyrites occurring in a fine-grained euhedral form are scattered in the carbonate rock. The early stage fractured pyrites are filled with galena veins and replaced by late-stage light-colored sphalerite with a metasomatic relict texture (Fig. 5-B). Fine-grained euhedral and foliated pyrites are exsolved in sphalerite (Fig. 5-C), resembling the exsolution texture. The ore body is primarily composed of dolomites or calcites with banded structures, as well as a few light-colored sphalerites (Fig. 5-D). The sediments exhibit concentric folds filled with interstitial material that is mainly composed of metal sulfides, such as pyrite, and precipitated dolomites or calcites. Lead–zinc sulfides fill the fractures of the dolomitized limestone, forming epigenetic breccia–conglomerate (Fig. 5-E). The observed flow structure suggests that structural deformation occurs during sedimentary mineralization (Fig. 5-F). Alternatively, the collapsed breccia (dolomite cemented with lead–zinc sulfides, Fig. 5-I) is likely formed by filling the dolomite fractures with lead–zinc sulfides, loading the stress onto the dolomitized surrounding rocks and forming jagged or angular dolomite edges (Fig. 5-G, H).

The alteration of the surrounding rocks is widespread and represented by dolomitization, calcitization, and silicification. Based on their textures and grain sizes, the dolomitized rocks can be classified as
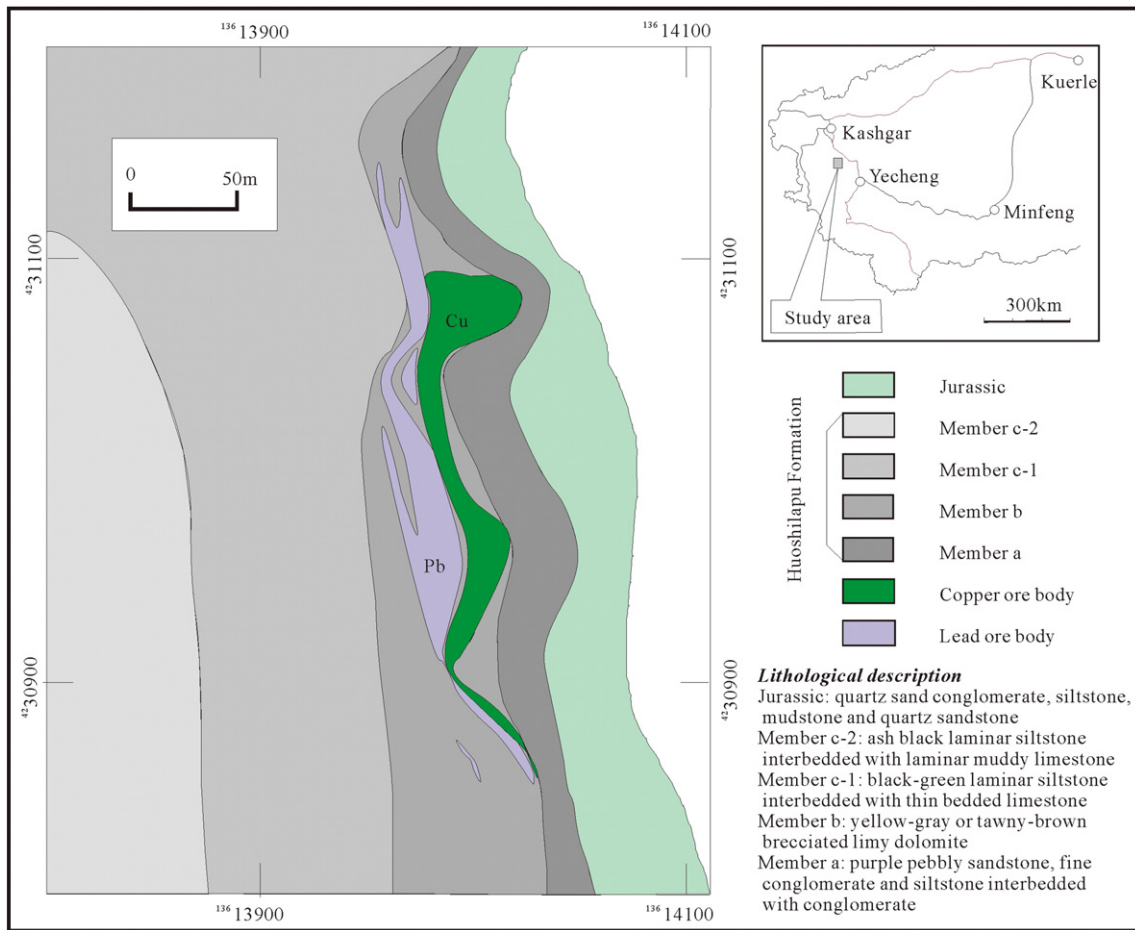
Fig. 8. Geological map of copper–lead deposits in Abalieke (edited after Zhang et al., 2011b).
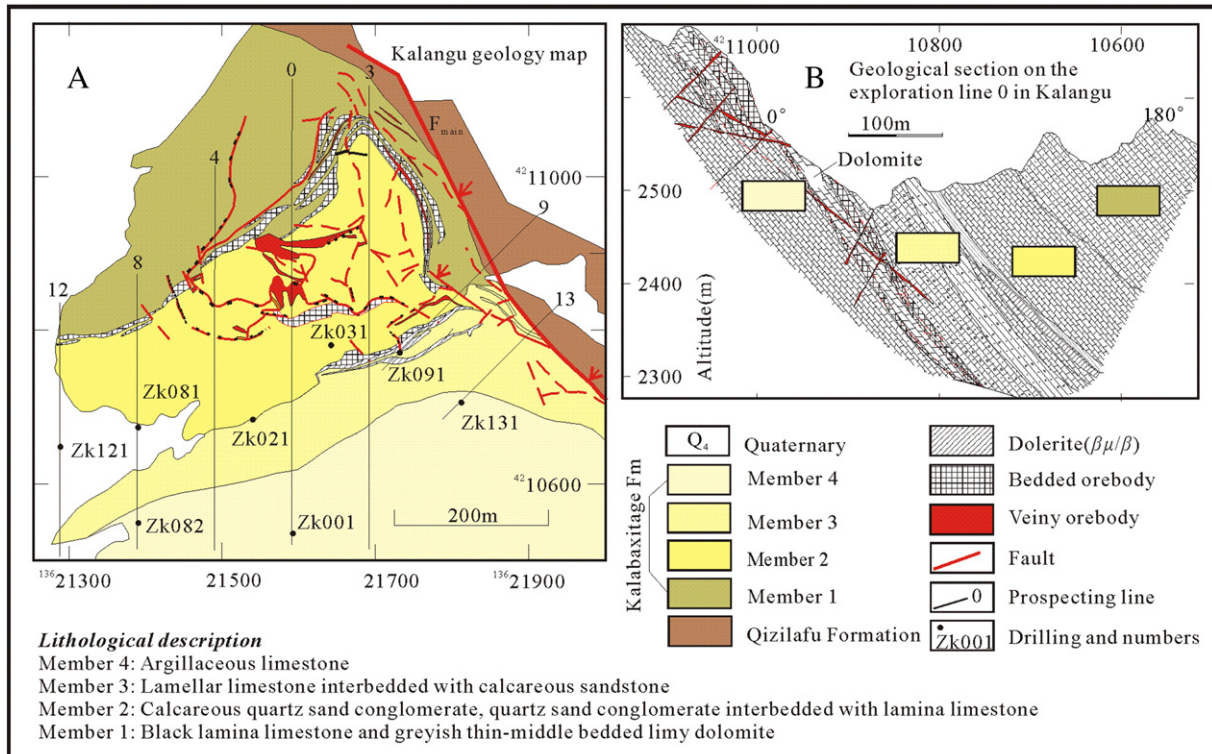

Fig. 9. Geological map of lead–zinc deposits (A) and cross-sectional map of the No. 0 prospecting line (B) in Kalangu (edited after Zhang et al., 2011a).

Table 2
Sulfur and lead isotope compositions and typical values of sulfide minerals from Pb–Zn–Cu deposits in polymetallic ore belt, western Kunlun.

Deposit	Sample no	Mineral	Grading	δ³⁴S‰	²⁰⁶Pb/²⁰⁴Pb	±2σ	²⁰⁷Pb/²⁰⁴Pb	±2σ	²⁰⁸Pb/²⁰⁴Pb	±2σ	T	μ	Th/U
Tiekelike	TKLK-10	Gn	Coarse	−7.6	18.028	0.001	15.697	0.001	38.439	0.003	553	9.71	3.95
	TKLK-23	Gn	Fine	−4.7	18.080	0.001	15.680	0.001	38.474	0.002	498	9.66	3.94
	TKLK-28	Gn	Fine	−8.5	18.021	0.001	15.687	0.001	38.397	0.003	547	9.69	3.94
	TKLK-32	Gn	Coarse	5.9	18.067	0.001	15.752	0.001	38.611	0.004	587	9.81	4.02
	TKLK-33	Cp	Coarse	7.6	18.000	0.001	15.628	0.001	38.583	0.002	494	9.57	4.02
	TKLK-37	Gn	Fine	7.1	18.029	0.002	15.705	0.002	38.463	0.005	561	9.72	3.97
	TKLK-38	Gn	Coarse	6.1	18.036	0.002	15.714	0.002	38.484	0.004	566	9.74	3.97
	TKLK-914	Gn	Coarse	−7.5	18.032	0.002	15.688	0.002	38.414	0.005	540	9.69	3.94
	TKLK-916	Cp	Fine	−4.6	18.013	0.001	15.603	0.001	38.201	0.002	456	9.52	3.84
	TKLK-917	Py	Fine	−5.7	17.980	0.001	15.604	0.001	38.145	0.002	481	9.52	3.84
	TKLK-918	Gn	Coarse	−7.6	18.035	0.002	15.693	0.002	38.435	0.004	544	9.70	3.95
	TKLK-919	Cp	Fine	8.0	18.141	0.001	15.615	0.001	38.404	0.002	379	9.52	3.87
	TKLK-921A	Gn	Coarse	5.3	18.020	0.002	15.692	0.002	38.407	0.004	561	9.72	3.96
	TKLK-921B	Gn	Coarse	−8.3	18.055	0.001	15.735	0.001	38.549	0.003	577	9.78	3.99
	TKLK-921C	Gn	Coarse	3.4	17.963	0.001	15.642	0	38.250	0.001	536	9.60	3.90
	TKLK-922	Cp	Fine	−5.3	17.977	0.001	15.598	0.001	38.349	0.002	476	9.51	3.93
Tamu	TM-807	Gn	Fine	3.9	17.992	0.001	15.638	0.001	38.316	0.003	512	9.59	3.91
	TM-809	Gn	Fine	2.8	17.994	0.002	15.643	0.002	38.323	0.005	516	9.60	3.91
	TM-810	Gn	Coarse	4.7	18.022	0.001	15.677	0.001	38.453	0.003	535	9.67	3.96
	TM-813	Gn	Fine	3.8	18.044	0.003	15.706	0.004	38.514	0.01	552	9.72	3.98
	TM-814	Gn	Fine	4.2	18.050	0.001	15.716	0.001	38.547	0.003	559	9.74	3.99
	TM-25	Gn	Coarse	4.3	18.010	0.001	15.661	0.001	38.380	0.002	525	9.63	3.94
	TM-37-1	Gn	Fine	2.8	18.012	0.001	15.663	0.001	38.377	0.001	526	9.64	3.93
	TM-901	Gn	Fine	−0.2	17.970	0.002	15.610	0.001	38.197	0.004	495	9.54	3.87
	TM-902	Gn	Coarse	4.9	17.987	0.001	15.631	0.001	38.268	0.002	507	9.58	3.89
	TM-916	Gn	Fine	4.5	18.008	0.001	15.661	0.001	38.369	0.002	526	9.63	3.93
	TM-918	Gn	Fine	4.3	17.983	0.001	15.627	0.001	38.263	0.002	505	9.57	3.89
	TM-929	Gn	Coarse	5.1	18.013	0.001	15.665	0.001	38.392	0.001	527	9.64	3.94
	TM-932	Gn	Coarse	−0.1	17.997	0.001	15.640	0.001	38.326	0.002	510	9.59	3.91
	TM-936	Gn	Fine	−1.8	17.974	0.001	15.620	0.001	38.252	0.003	504	9.56	3.89
	TM-938	Gn	Coarse	4.9	18.032	0.004	15.694	0.004	38.483	0.011	547	9.70	3.97
	TM-944	Gn	Coarse	1.4	18.007	0.002	15.655	0.002	38.336	0.006	520	9.62	3.92
	TM-947	Gn	Fine	0.6	18.024	0.002	15.679	0.002	38.437	0.004	536	9.67	3.95
	TM-948	Gn	Coarse	5.5	18.049	0.002	15.712	0.002	38.532	0.004	555	9.73	3.99
Abalieke	ABLK-708	Cp	Fine	24.0	17.966	0.001	15.600	0.001	38.172	0.001	486	9.52	3.85
	ABLK-709	Cp	Coarse	−30.7	18.046	0.001	15.599	0.001	38.186	0.002	428	9.5	3.82
	ABLK-713	Cp	Coarse	−28.1	17.978	0.001	15.601	0.001	38.195	0.003	479	9.52	3.86
	ABLK-720	Gn	Fine	−30.8	17.994	0.002	15.652	0.002	38.357	0.005	526	9.62	3.93
	ABLK-727	Cp	Coarse	−28.1	17.972	0.001	15.607	0.001	38.210	0.003	490	9.53	3.87
	ABLK-829	Cp	Coarse	−29.5	18.096	0.001	15.604	0.001	38.171	0.003	399	9.51	3.78
	ABLK-903A	Cp	Coarse	−25.4	18.144	0.001	15.608	0.001	38.221	0.002	369	9.51	3.78
	ABLK-917	Gn	Fine	−25.8	17.969	0.003	15.646	0.004	38.325	0.010	537	9.61	3.93
	ABLK-933	Cp	Coarse	−32.0	18.019	0.001	15.609	0.001	38.251	0.002	459	9.53	3.86
	ABLK-934	Cp	Coarse	−38.3	18.058	0.001	15.599	0.001	38.220	0.002	425	9.53	3.84
	ABLK-937	Cp	Coarse	−36.0	17.946	0.001	15.614	0.001	38.280	0.003	516	9.55	3.92
Kalangu	KLG-12	Gn	Fine	−7.3	18.048	0.002	15.702	0.002	38.550	0.004	545	9.71	3.99
	KLG-I-901	Gn	Fine	−9.1	18.014	0.004	15.716	0.005	38.645	0.012	584	9.75	4.06
	KLGX-902	Gn	Coarse	−5.5	17.994	0.004	15.705	0.004	38.556	0.009	585	9.73	4.03
	KLGX-905	Gn	Coarse	−13.6	17.975	0.001	15.675	0.001	38.490	0.002	565	9.67	4.00

Explanations: Gn—galena; Cp—chalcopyrite; Py—pyrite; TKLK—Tiekelike; ABLK—Abalieke; TM—Tamu; KLG—Kalangu.
The samples were collected respectively from the main ore body of the Tiekelike, Abalieke, Tamu and Kalangu deposits.

fine- to medium-grained, thick massive dolomites, and dolomitized limestone. All of these forms are closely related to lead–zinc mineralization; the limy dolomites exhibit the highest grade. The calcitized rocks are in reticular and granular forms; they are widely distributed in the surrounding rocks (Yang, 2009). The silicification process is closely related to sulfides and generally occurs within limestone and dolomite faults in netty, granular, and disseminated forms.

3.3. Abalieke copper–lead deposit

The Abalieke copper–lead deposit is located between the lower clastic rocks and the upper carbonate members of the Huoshilafu Formation (Fig. 1-B, Table 1). The ore-bearing hosting rock is completely dolomitized and exhibits only a brecciated appearance without preserving the original beddings. The ore bodies occur as lenses and sheets, and isolated ore bodies are observed where the superimposition occurred over multiple stages (Fig. 8).

The Cu–Pb ore body is approximately 300 m long and 5–15 m wide (with a maximum width up to 30 m), with a confirmed depth of 100 m. The surrounding rocks are brown clastic and dark gray dolomite intercalated with brecciated dolomite. The breccia includes mostly dark dolomite less than 4 cm in diameter. A small amount of quartz from the quartz conglomerate and the pebbly quartz sandstone occurs in the footwall of the ore body. The cements consist of dolomite, fine-grained muddy debris, and sulfides. The ore contains mostly chalcopyrite in dolomite breccias, as well as more than 5% copper. The ore body has a N strike with a 40° dipping orientation. Copper mineralization occurs primarily along the interface between the clastic and dolomitic limestone in the lower rock formation, while lead mostly occurs in the upper dolomitic limestone.
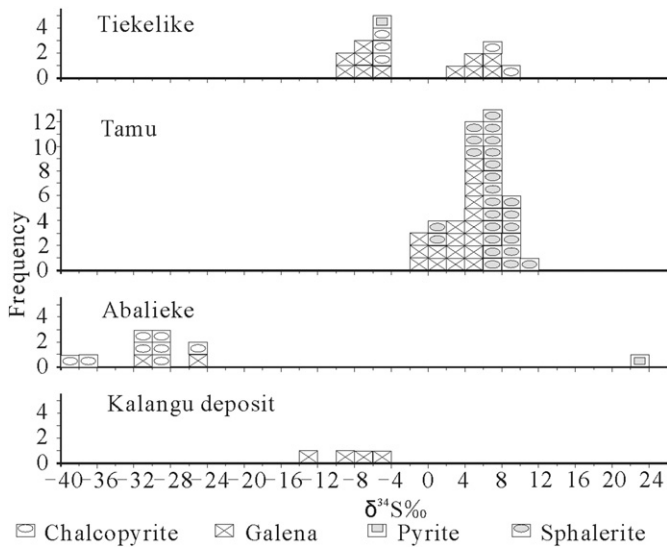
Fig. 10. Histogram of sulfur isotope of sulfide minerals from the deposits near the western Kunlun mountains in China.

The major minerals include chalcopyrite, galena, pyrite, and a small amount of sphalerite. The average lead and copper contents are 2.06% and 0.84%, respectively, and increase with depth.

The ore textures are framboidal, lattice, and euhedral. The pyrite forms during the early stages and is distributed in a framboidal texture (Fig. 4-G); however, the metasomatic fine-grained galena forms in carbonate fissures. Chalcopyrite and sphalerite have a latticed structure (Fig. 4-H) resembling an exsolution structure. The chalcopyrite formed during the early stage is replaced by euhedral pyrite (metasomatic residual texture, Fig. 4-I), forming the chalcopyrite residue. The dolomite breccias exhibit brecciated structure (Fig. 4-J) with sharper edges. The bornite is replaced by chalcopyrite, exhibiting metasomatic texture (Fig. 4-K). The chalcopyrite veins filling the dolomitic limestone form the massive structure (Fig. 4-L).

3.4. Kalangu lead deposit

The deposit is located in a fault zone within the upper Devonian Qizilafu Formation and the lower Carboniferous Kelitage Formation

(Fig. 1-B, Table 1, Fig. 9A). The fault zone has an overall NE strike and a dip to the SE. The hanging wall of the fault consists of carbonate from the Kelitage Formation, while the footwall is brown sandstone from the Qizilafu Formation. The fault is a high angle thrust (60°) with varying degrees of brecciation. The ore is generally distributed along the bedding planes, with some layering. The ore body crops out with an average thickness of 28 m. The footwall rock of the ore body is thinly bedded dolomitic limestone, while the hanging wall contains quartz gravel carbonate or off-white calcareous quartz glutenite. The galena occurs in the cataclastic dolomite of the second member with almost uniform distribution within the formation (Fig. 9 B).

The ore occurs mainly in disseminated, veinlet, and massive structures. The ore minerals include mostly galena, followed by chalcopyrite, pyrite, sphalerite, and trace amounts of maucherite. The secondary minerals include malachite, covellite, chalcocite, erythrite, cerussite, and limonite.

The ore exhibits in heterogranular, skeletal and metasomatic dissolution textures, and disseminated and filled veinlet structures. Granular pyrite is disseminated in sandstone (Fig. 5-J). The granular pyrite and galena are mostly interspersed (Fig. 5-K). The petrographic evidence suggests that the sphalerites likely formed in two stages (Fig. 5-L): the stage I sphalerite (Sph-I) appears beige under a microscope and is darker than the later stage II sphalerite (Sph-II). The sphalerites are formed later than the pyrite and are replaced by late stage chalcopyrite via dissolution (You et al., 2012). The stage II sphalerite intruded into the chalcopyrite as veins. The pyrite exhibits a skeletal texture (Fig. 5-M). The galena fills the dolomitic limestone, separating the dolomitic limestone with galena veins in a filling texture (Fig. 5-N). The calcite and clastic silt are interstitial materials that generate veins in the dolomitic limestone, while the calcite exhibits rhombohedral cleavage in the veins (Fig. 5-O).

4. Geochemistry of the deposits

4.1. Sulfur isotopes

Samples of galena, sphalerite, pyrite, and chalcopyrite were collected from the Tiekelike, Tamu, Abalieke, and Kalangu deposits. The samples were analyzed at the Institute of Geochemistry at the Chinese Academy of Sciences using a continuous flow isotope ratio mass spectrometer (CF-IRMS) (EA-IsoPrime, EA: Euro3000, IRMS: GV Instruments). The isotopic sulfur data are presented in delta over the Canyon Diablo Troilite standard value. The sulfur isotope standards
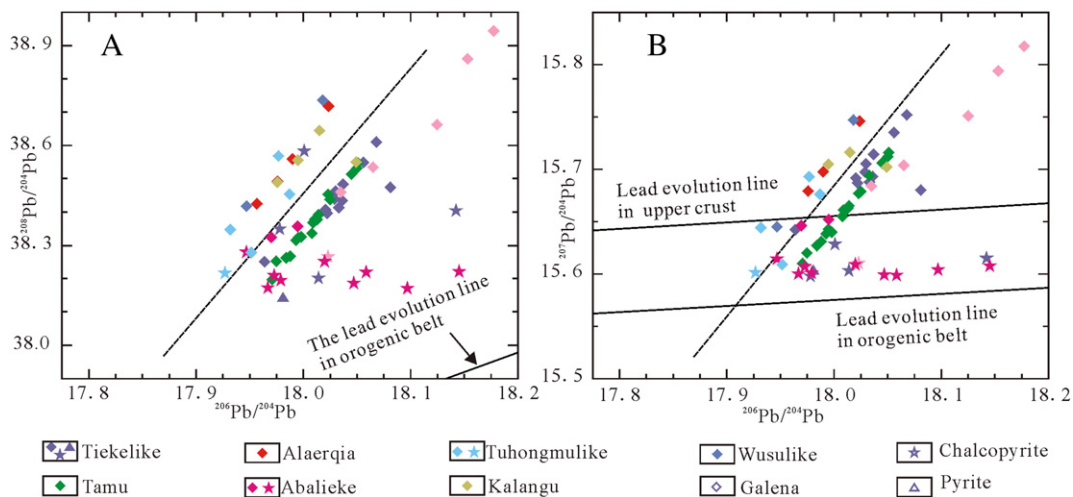

Fig. 11. Isotopic lead compositions for the sulfide minerals from the Pb–Zn–Cu deposits in western Kunlun, China (lead evolution curves adopted from Zartman and Doe, 1981). (A) Binary correlation diagrams of $^{206}Pb/^{204}Pb–^{208}Pb/^{204}Pb$; (B) Binary correlation diagrams of $^{206}Pb/^{204}Pb–^{207}Pb/^{204}Pb$.

Table 3
Rb–Sr isotopic composition of the fluid inclusions within sphalerite in Tamu deposit, western Kunlun.

Sample no	Test object	Rb($\times 10^{-6}$)	Sr($\times 10^{-6}$)	^{87}Rb/^{86}Sr	^{87}Sr/^{86}Sr	t(Ma)	(^{87}Sr/^{86}Sr)$_i$
RO-4	Brecciated stuff	1.4060	213.5000	0.0189	0.70995 ± 0.00009		
DO-4	Cements	0.4786	335.9000	0.0041	0.70995 ± 0.00005		
BS-8*	Stabilites	0.0478	1.2000	0.1149	0.71148 ± 0.00003		
DB-4	Leach residue	0.1852	0.4518	1.1830	0.71659 ± 0.00022	386.30	0.71008
DB-4	Lixivium	0.0358	20.3000	0.0050	0.71011 ± 0.00008		
DB-4	Stabilites	0.1710	20.5800	0.0239	0.71023 ± 0.00001		
DB-6	Leach residue	0.2100	0.5274	1.1480	0.71338 ± 0.00018	193.20	0.71023
DB-6	Lixivium	0.0417	24.1400	0.0049	0.71024 ± 0.00002		
DB-6	Stabilites	0.1733	27.4400	0.0182	0.71009 ± 0.00003		
DB-8	Leach residue	0.2166	0.4114	1.5190	0.71479 ± 0.00015	213.00	0.71019
DB-8	Lixivium	0.0500	21.1300	0.0068	0.71021 ± 0.00005		
DB-8	Stabilites	0.1887	19.5700	0.0278	0.71025 ± 0.00004		
DG-4	Leach residue	0.1428	0.2459	1.6760	0.71842 ± 0.00013	343.10	0.71023
DG-4	Lixivium	0.0395	12.1300	0.0094	0.71028 ± 0.00001		
DG-4	Stabilites	0.1164	14.5600	0.0230	0.71042 ± 0.00001		
DG-6	Leach residue	0.1092	0.2751	1.1450	0.71542 ± 0.00014	320.20	0.71020
DG-6	Lixivium	0.0371	17.5700	0.0061	0.71023 ± 0.00005		
DG-6	Stabilites	0.09351	19.8800	0.0135	0.71022 ± 0.00001		

Explanations: The samples were collected from the main ore body of the Tamu deposits (Yang, 2009).

(GBW04414 (Ag$_2$S, δ^{34}S$_{CDT}$ = −0.07 ± 0.13‰) and GBW04415 (Ag$_2$S, δ^{34}S$_{CDT}$ = +22.15 ± 0.14‰)) have measurement errors below ± 0.2‰ (2σ). The analytical results are listed in Table 2 and are shown in Fig. 10.

The δ^{34}S values of the sulfide minerals range from −38.3‰ to +24.0‰ with two major distribution ranges: −13.6‰ to +24.0‰ and −38.3‰ to −12.0‰. The isotopic values vary among the sulfides with a general decreasing trend: δ^{34}S$_{Sph}$ > δ^{34}S$_{Gn}$ > δ^{34}S$_{Py}$ > δ^{34}S$_{Ccp}$. Therefore, the isotopic ratios in most samples have reached equilibrium. The δ^{34}S values for the Tamu, Tiekelike, and Kalangu deposits mostly range from −6.0‰ to +6.0‰, while the Abalieke deposit has negative δ^{34}S values covering a wide range (−32.0‰ to −24.0‰). The other ore deposits nearby show a similar pattern with the studied deposits (You et al., 2011; Zhu et al., 1998).

4.2. Lead isotopes

The lead isotopes were analyzed in samples of galena, pyrite, and chalcopyrite from the Tamu, Tiekelike, Kalangu, and Abalieke deposits. These analyses were conducted at the Beijing Research Institute of Uranium Geology using ISOPROBE-T thermal ionization mass spectrometry. The measured lead isotope ratios are listed in Table 2.

Compared to the other ore deposits in the region (Shen et al., 2012), the galena samples contain ^{206}Pb/^{204}Pb of 17.931–18.176 (mean = 18.017), ^{207}Pb/^{204}Pb of 15.609–15.818 (mean = 15.684), and ^{208}Pb/^{204}Pb of 38.197–38.944 (mean = 38.462). The chalcopyrite samples have ^{206}Pb/^{204}Pb of 17.926–18.144 (mean = 18.020), ^{207}Pb/^{204}Pb of 15.598–15.628 (mean = 15.606), and ^{208}Pb/^{204}Pb of 38.171–38.583 (mean = 38.262). The pyrite sample has ^{206}Pb/^{204}Pb of 17.980, ^{207}Pb/^{204}Pb of 15.604, and ^{208}Pb/^{204}Pb of 38.145. After plotting the data (Fig. 11), the figure shows that the lead isotope levels for the sulfide minerals lie above the lead evolution line for the western Kunlun orogeny and within the lead evolution line for the upper crust origin. Most of the lead isotope data from chalcopyrite are slightly above the lead evolution line of the western Kunlun orogeny and show a near linear relationship, indicating that these samples only represent source regions with different ^{238}U/^{204}Pb values; the mixing of normal lead from different sources may be minimal. Furthermore, because the data lie above the evolution line of the upper crust, the Pb might form in an environment with rising ^{232}Th/^{204}Pb and ^{238}U/^{204}Pb over long periods (Shen et al., 2012). Therefore, the Pb isotope compositions indicate that Pb might also originate from sources other than the upper crust, such as the basement of the western Kunlun orogeny, as suggested by Zhu et al. (1998).

4.3. Strontium isotopes

Twelve sphalerite samples with different granules and colors (dark black, dark green, dark yellow, and bright yellow) from the Tamu Pb–Zn deposit were analyzed at the Isotope Laboratory of the Yichang Institute of Geology and Mineral Resources using a Rb–Sr dating method for the fluid inclusions in sphalerite, as described by Nakai et al. (1990; 1993). The results are listed in Table 3 and Fig. 12. Isochrone dating using an Isoplot 3.66 Model-3 analysis (Ludwig, 1994) estimates the age as 337 Ma, the (^{87}Sr/^{86}Sr)$_i$ ratio as 0.71020, correlation coefficient (R) as 0.9981, and MSWD as 12. Isochrone dating using Model-1 analysis (Ludwig, 1994) provides an age of 337 Ma, a (^{87}Sr/^{86}Sr)$_i$ ratio of 0.71020, and an MSWD of 3. Isochrone dating using the GeoKit method (Lu, 2004) generates an age of 336.7 ± 7.4 Ma, a (^{87}Sr/^{86}Sr)$_i$ ratio of 0.71020, and an R of 0.9990. The strontium isotope data suggest that the sphalerites formed during the early Carboniferous period (Yang, 2009).

4.4. Rhenium–Osmium isotopes

Seven chalcopyrite samples and one pyrite sample from the main ore body of the Abalieke Cu–Pb deposit were selected for Re–Os isotope analysis using an ICP-MS method documented by Qi et al. (2007). The sensitivity of the PE ELAN DRC-e was adjusted to approximately 30,000 cps for 1 ng ml^{-1} of ^{103}Rh. Most results yield relative standard deviations (RSDs) of <5% for the ^{187}Os/^{190}Os ratios, and duplicate analyses using the same individual samples yield consistent results. The
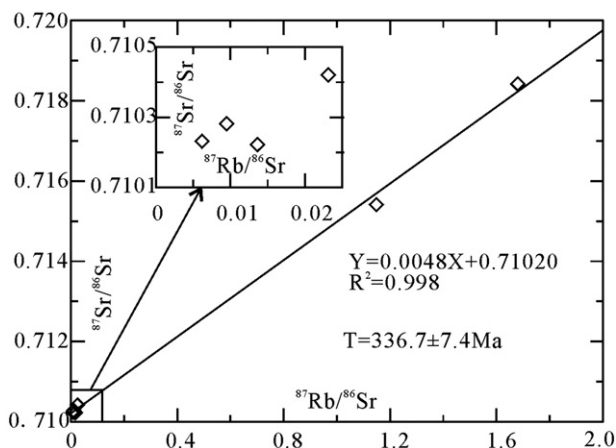

Fig. 12. Rb–Sr isotopic age determination in fluid inclusions within the sphalerite in the Tamu deposit.

Table 4
Re, Os isotopic composition of chalcopyrite and pyrite in Abalieke and Tiekelike deposit, western Kunlun.

Sample no	Test mineral	^{187}Re	^{187}Re 1σ	^{187}Os	^{187}Os 1σ	Re (ng/g)	Re(ng/g) 1σ	Common Os(ng/g)	Common Os(ng/g) 1σ	Model age (Ma)	Model age (Ma) 1σ
ABLK-909	Chalcopyrite	1697	23	9.3700	0.1200	2711	37.00	0.3600	0.0200	331.59	4.13
ABLK-929	Pyrite	392	10	2.2200	0.0900	626	16.00	0.0610	0.0110	340.74	13.59
ABLK-931	Chalcopyrite	4643	120	25.4000	0.2600	7417	191.00	0.1400	0.0300	328.36	3.31
ABLK-934	Chalcopyrite	4264	70	23.4700	0.3600	6811	112.00	0.2100	0.0600	330.74	5.11
ABLK-939	Chalcopyrite	9097	129	49.1200	0.5100	14533	206.00	0.2100	0.0200	324.39	3.37
ABLK-932	Chalcopyrite	4690	63	26.2200	0.3100	7492	100.00	0.0330	0.0300	335.80	5.40
ABLK-933	Chalcopyrite	5026	32	27.9300	0.2000	8029	51.00	0.0260	0.0190	333.80	2.60
ABLK-944	Chalcopyrite	3719	30	21.0300	0.2300	5941	48.00	0.2020	0.0270	339.70	3.20
TKLK-916	Chalcopyrite	1.999	0.027	0.0070	0.0004	3.19	0.04	0.0051	0.0017	210.10	10.20

Explanations: TKLK—Tiekelike; ABLK—Abalieke
The samples were collected from the main ore body of the Tiekelike and Abalieke deposits.

total procedure blanks for Re and Os were approximately 6.4 ± 1.1 pg and 2.0 ± 0.4 pg, respectively. Iridium was added to the Re- and Os-bearing solution for a mass discrimination correction. The rhenium–osmium isotope results are listed in Table 4 and presented in isochrone charts, as shown in Fig. 13, after using the ISOPLOT program (Ludwig, 1994). These samples have high Re and low Os levels, as well as a high Re/Os ratio and a high ^{187}Os/^{188}Os ratio. The samples contain 626–14533 ng of Re and 0.026–0.36 ng of Os; isochrone dating using ISOPLOT analysis (Ludwig, 1994) indicates that their isochrone age is Hercynian (331.3 ± 5.2 Ma), corresponding to the ore-bearing surrounding rocks of the Abalieke Cu–Pb deposits (lower Carboniferous stage, 354–320 Ma), indicating a syn-depositional mineralization.

4.5. Argon isotopes

Samples of the quartz from the coarse-grained massive ore in the Kalangu deposit were used for argon dating. Because quartz and the closely associated lead–zinc sulfide minerals most likely formed at the same time, the age of the sulfide might be estimated from the Ar isotope data for the quartz. The selected mono-mineral quartz samples were analyzed at the Guangzhou Institute of Geochemistry at the Chinese Academy of Sciences using a 5400Ar® mass spectrometer by GV Instruments (UK) and a COHERENT-50 W carbon dioxide laser by Shenzhen Lightstar Laser Technology Co., Ltd. (China). The Ar dating data were processed using the ArArCALC software v.2.40 (Koppers, 2002); the results are presented in Table 5 and shown in Fig. 14. The Ar–Ar plateau age and the isochrone age of the quartz in the Kalangu Pb deposit were both 235 Ma.

4.6. Fluid inclusions

The ore bodies of the Tiekelike, Abalieke, and Kalangu deposits all contained quartz. However, the Zn–Pb ore bodies of the Tamu deposit contain very little quartz and relatively abundant sparry dolomite

Fig. 13. Re–Os isotopic dating in the chalcopyrite and pyrite in the Abalieke deposit of western Kunlun.

containing primary fluid inclusions. Therefore, while the study focused on the fluid inclusions in the quartz, the fluid inclusions in the sparry dolomite (Fig. 15) were also analyzed. The fluid inclusion data are listed in Table 6.

The calculated pressure ranges from 33 to 65 MPa, and the corresponding average mineralization depth ranges from 5.85 to 4.24 km, corresponding to epithermal deposits (Feng et al., 2009). The salinity values (NaCl) of the Tiekelike, Abalieke, and Kalangu are similar (12% to 20%), while the salinity of Tamu is lower (6% to 12%). The total fluid inclusion densities are approximately 1.0 g/cm^3. The homogenization temperature, salinity, and density data (Fig. 16) suggest a medium-low salinity, a medium-low temperature, and a medium density hydro-thermal fluid.

5. Discussion

5.1. Deposit features indicate two stages of mineralization

Except for some secondary minerals that were formed through the oxidation of primary sulfide minerals, most ore minerals can be classified as depositional and transformational based on their assemblage and texture (Fig. 17).

The depositional mineralization formed early stage pyrite and granular galena in stratoid, disseminated, and dense massive forms. The framboidal texture of the pyrite and banded structure of metal sulfides indicates that it might have a biogenic or an epithermal origin similar to the mineralization of stratabound sedimentary deposits (Tu, 1984; Wolf, 1976). The banded texture of the metal sulfides suggests characteristics similar to depositional ores (Wolf, 1976). After diagenesis, the pyrite exhibits disseminated euhedral and granular textures in carbonate and sandstone. The dolomitization, silicification, sulfation, and desulfation within stratoid orebody indicate that the minerals underwent early stage metasomatism.

The late stage pyrite and coarse-grained euhedral galena formed during the transformational mineralization, producing irregular ore bodies consisting of vein, mesh-veiny, and massive ores. The brecciated, veiny, and flow structures were common during the filling stage. Because the hydrothermal fluid interacted with the sedimentary rock during the transformational stage, early ore minerals might be dissolved in the stratiform ore bodies; afterward, they may precipitate as into veins in the fault zone near the stratiform ore bodies. The intense tectonic events caused fluid movement and interactions between the fluid and the surrounding rock. Two modes of transformational mineralization are known. The metasomatism between the hydrothermal fluid and the sedimentary rock occurs within the stratiform ore body, while the stratiform texture is largely preserved. Chalcopyrite is often corroded and replaced by galena, pyrite, and sphalerite, forming a residual metasomatic texture. Tectonic stresses might also induce folding and faults in the ore-bearing strata, enabling hydrothermal fluid migration along the fissures to corrode the ore-bearing carbonate and form the metasomatic and skeletal texture in the second mineralization model. The fractures of carbonate that formed under tectonic stress develop an angular or
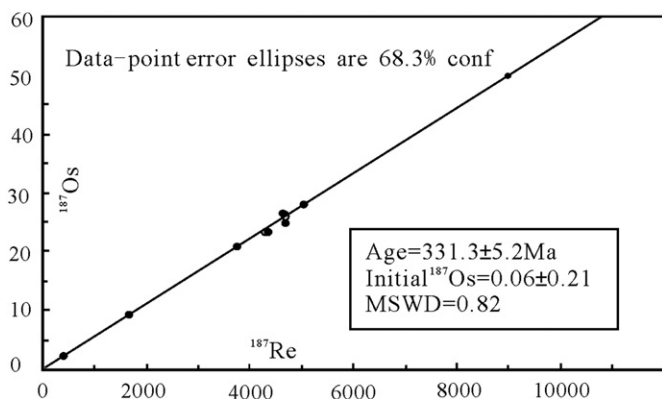
Table 5
Ar–Ar isotopic data from quartz in Kalangu Zn–Pb deposit, western Kunlun.

Incremental heating		$^{36}Ar(a)$	$^{37}Ar(ca)$	$^{38}Ar(cl)$	$^{39}Ar(k)$	$^{40}Ar(r)$	Age ± 1 s (Ma)	$^{40}Ar(r)$ (%)	$^{39}Ar(k)$ (%)	K/Ca ± 1 s
10G2192B	10 °C	0.011308	0.000290	0.000141	0.000029	1.228235	8641.64 ± 190.81	15.24	1.46	0.044 ± 0.006
10G2192C	15 °C	0.008084	0.000338	0.000092	0.000050	0.943178	7248.10 ± 173.71	16.19	2.44	0.063 ± 0.007
10G2192D	25 °C	0.005684	0.000562	0.000061	0.000042	0.720952	7044.70 ± 212.43	17.35	2.10	0.032 ± 0.004
10G2192E	40 °C	0.004380	0.000988	0.000049	0.000036	0.588620	6982.45 ± 205.03	18.20	1.77	0.016 ± 0.002
10G2192F	80 °C	0.004399	0.002035	0.000047	0.000032	0.566364	7103.98 ± 139.86	17.57	1.59	0.007 ± 0.001
10G2192G	160 °C	0.004088	0.004976	0.000039	0.000117	0.498012	4655.53 ± 81.74	16.78	5.77	0.010 ± 0.001
10G2192I	240 °C	0.003161	0.008520	0.000027	0.000117	0.365594	4139.06 ± 71.97	16.07	5.80	0.006 ± 0.001
10G2192J	360 °C	0.002487	0.015250	0.000027	0.000094	0.278703	4057.41 ± 77.25	15.65	4.65	0.003 ± 0.000
10G2192K	480 °C	0.001908	0.019349	0.000017	0.000174	0.184193	2518.39 ± 74.74	13.78	8.57	0.004 ± 0.000
10G2192L	600 °C	0.001422	0.021031	0.000014	0.000148	0.117497	2135.92 ± 76.76	12.03	7.33	0.003 ± 0.000
10G2192M	720 °C	0.001073	0.020157	0.000005	0.000196	0.081495	1414.65 ± 66.87	11.16	9.68	0.004 ± 0.000
10G2192N	760 °C	0.000915	0.015904	0.000003	0.000155	0.008774	271.27 ± 136.39	1.56	7.64	0.004 ± 0.000
10G2192O	720 °C	0.000654	0.010549	0.000008	0.000239	0.010881	221.43 ± 77.27	2.68	11.78	0.010 ± 0.001
10G2192Q	720 °C	0.000483	0.007097	0.000001	0.000200	0.010022	242.36 ± 62.05	3.32	9.85	0.012 ± 0.001
10G2192R	720 °C	0.000423	0.005229	0.000004	0.000238	0.011704	237.63 ± 46.32	4.38	11.75	0.020 ± 0.001
10G2192S	720 °C	0.000351	0.003636	0.000004	0.000096	0.004502	228.41 ± 89.77	2.08	4.71	0.011 ± 0.001
10G2192T	720 °C	0.000307	0.002793	0.000003	0.000063	0.002326	180.82 ± 180.90	1.24	3.12	0.010 ± 0.001

Explanations: The samples were collected from the main ore body of the Kalangu deposit.

jagged shape to form catagenetic breccias. Concurrently, the tectonic movement provided the kinetic conditions for the deposition and mineralization of metal sulfides similar to the mineralization of orogenic deposits (Chen et al., 2000).

5.2. Multi-faceted ore-forming materials

In agreement with previous reports (Feng et al., 2009; Kuang et al., 2002; Wang et al., 2001), our studies on the fluid inclusions (Figs. 15 and 16, Table 6) reveal that the formation of a Pb–Zn deposit in the Tamu–Kalangu zone involves fluids from two or more sources. The δD–$\delta^{18}O$ diagrams show that the water in the ore-forming fluids originates from precipitated meteoric water. The composition of the fluid inclusion shows two opposing end-members: the oxidative and reductive environments. The characteristics of the enriched Ca^{2+}, Mg^{2+}, and HCO_3^- ions in this study differ from the typical characteristics of MVT deposits, as described by Anderson (1975).

The sulfur isotope data indicate the presence of two different ore-forming hydrothermal fluids during mineralization: a reducing hydrothermal fluid with a low $\delta^{34}S$ value between −29.3‰ and −17‰ and an oxidizing hydrothermal fluid poor in sulfur, rich in metal, and with high $\delta^{34}S$ values (−3.6‰ and +5‰). The former could react with the Fe, Zn, Pb, and Cu in the surrounding rocks to form early stage

disseminated and framboidal pyrite, as well as the fine-grained disseminated galena. The $\delta^{34}S$ values might also describe the lithology and texture of the ores. For example, ores with very low $\delta^{34}S$ values from coarse clastic have fine-grained, framboidal spherical, and cemented textures, as well as a disseminated structure. In contrast, ores with high $\delta^{34}S$ values from dolomitized carbonate or the fault zone have crystalline, coarse-grained, and vein textures in a brecciated structure. Therefore, ores with different lithologies have different $\delta^{34}S$ values, reflecting the complexity of the sulfur sources.

The evolution curve for the lead isotopes is linear (Fig. 11), but its slope is independent of the age of the ore due to the incomplete mixing of two common Pb sources (Zhu et al., 1998). Additionally, the relatively limited Pb isotope composition and the fact that the Pb is older than the surrounding ore-bearing rocks characterize "B-type" Pb, as well as indicate the transportational sedimentary mineralization process for uranium and thorium after detachment from the terrigenous basement. Therefore, the positive linear correlation between the compositions of Pb isotopes in galena samples may be caused by the mixing of two types of Pb sources and might not be significant regarding the one- and two-stage Pb–Pb isochrone. The Pb might originate from both the upper crust and western Kunlun orogenic belt basement (Zhu et al., 1998). The measured age of the Pb isotope is pre-Devonian, indicating that the ore is from the basement of the ore-bearing rocks (Kuang et al., 2002).

Brown and Maryland (1970) argued that the MVT Pb–Zn deposits have very different Pb isotope compositions compared to the normal hydrothermal deposits, as characterized by their abundant radiogenic Pb. Leach et al. (2005) reached a similar conclusion after studying the Pb isotopes in sulfide samples from 30 MVT deposits. However, some researchers suggested that the Pb isotope characteristics of the MVT Pb–Zn deposits indicate multiple Pb sources, such as the J-type, B-type, and normal Pb (Brown and Maryland, 1970; Cannon et al., 1963; Leach et al., 2005). In contrast to the typical Pb signature in MVT deposits (Heyl et al., 1966), the sulfide minerals in western Kunlun have low $^{206}Pb/^{204}Pb$ (<18.2) and $^{208}Pb/^{204}Pb$ (<38.7), indicating that they have multiple Pb sources.

5.3. Mineralization stages and metallogenic model

Four mineralization ages reflecting two mineralization stages have been identified in this study: (1) the ages of the Rb–Sr isochrone of sphalerite in the Tamu deposit (337 Ma) and the Re–Os isochrone of chalcopyrite in the Abalieke deposit (331 Ma) are similar to those of the ore-bearing strata, suggesting syndepositional sedimentary
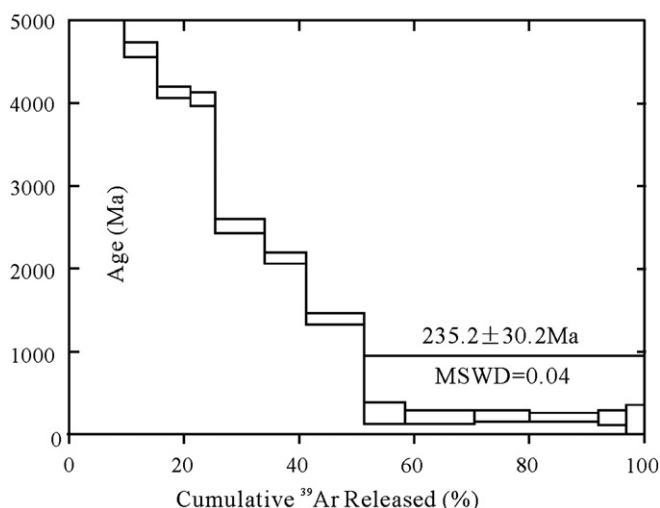

Fig. 14. Ar–Ar isotopic plateau age within the quartz in the Tamu Zn–Pb deposit.
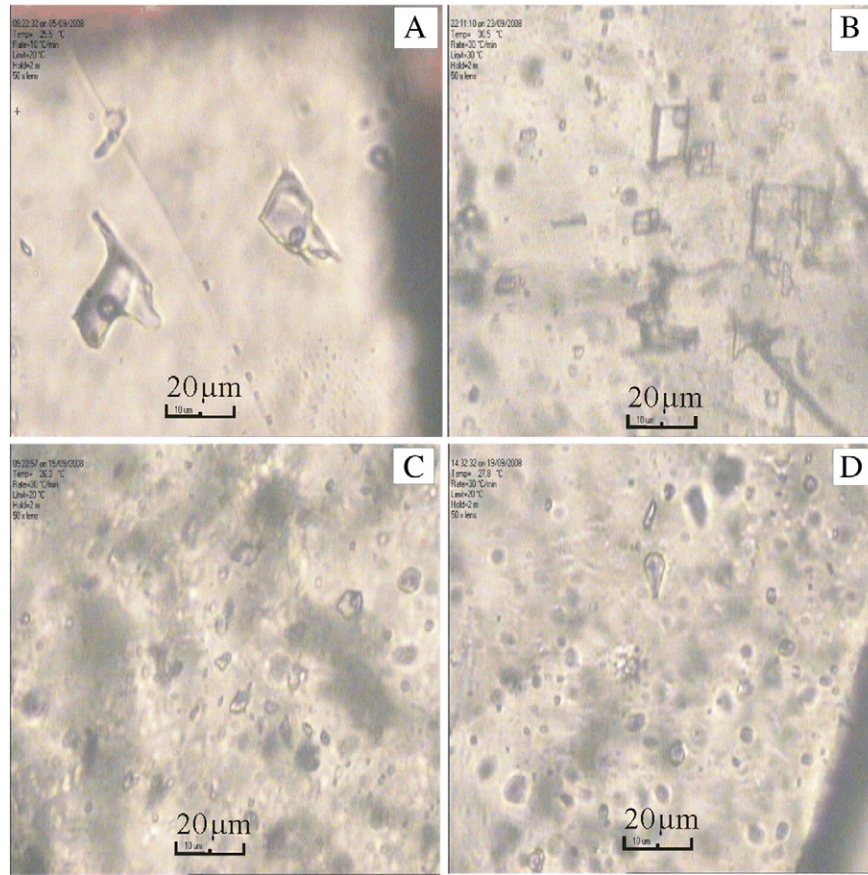
Fig. 15. Microscopic photographs of fluid inclusions in the Tiekelike (A), Tamu (B), Abalieke (C), and Kalangu (D) deposits. a — quartz in the Tiekelike deposit; b — dolomite in the Tamu deposit; c — quartz in the Abalieke deposit; d — quartz in the Kalangu deposit.

mineralization; (2) the Ar–Ar isochrone ages for the quartz in the Kalangu deposit (235 Ma) and the modeled Re–Os age of the chalcopyrite in the Tiekelike deposit (206 Ma) suggest that mineralization occurred during the orogenic uplift stages from the late Paleozoic era to the Triassic era. Due to the geochemical and geological characteristics of the deposit, we propose syndeposition and deformational mineralization models, as shown in Fig. 18.

The syndepositional mineralization occurred during the Devonian and early Carboniferous eras. The ore-bearing strata were located in a late Paleozoic subsiding basin at the south-west margin of the Tarim platform. Multiple basins were developed, and the syn-depositional faults developed along the margins (Fig. 18-A). A tectonic breccia belt with disordered stratigraphy formed under the anti-fault action accompanying the syn-depositional fault.

Table 6
Formation temperature of the fluid inclusions in Tiekelike, Tamu, Abalieke and Kalangu deposits.

Sample no	Determine quantity	Th(°C)	Tm(°C)	Vapor-liquid ratio (%)	Grain (µm)	Mineral	Salinity wt% NaCl eq.	Density g/cm^3
TKLK-25	21	148–280	−13.0 to −2.6	5–10	3–8	Quartz	4.3–16.9	0.87–1.02
TKLK-36	14	131–199	−16.7 to −5.9	5–10	3–12	Quartz	9.1–20.0	0.97–1.08
TKLK-28	18	153–229	−21.2 to −1.2	5–10	2–6	Quartz	2.1–23.2	0.91–1.05
TKLK-38	20	176–233	−14.8 to −4.8	5–10	4–13	Quartz	7.5–18.5	0.91–1.03
TKLK-15	18	180–250	−12.0 to −5.3	5–10	3–12	Quartz	8.3–16.0	0.92–0.96
TKLK-35	13	177–301	−17.5 to −6.9	5–10	7–15	Quartz	10.4–20.6	0.88–1.04
ABLK-36	21	134–230	−17.1 to −1.3	5–10	5–10	Quartz	2.3–20.3	0.92–1.04
ABLK-9	12	135–200	−13.9 to −3.5	5–10	4–5	Quartz	5.7–17.7	0.94–1.06
ABLK-01	22	125–180	−17.7 to −3.8	5–20	4–10	Quartz	6.1–20.5	0.96–1.05
ABLK-02	16	126–205	−15.8 to −3.8	5–10	4–6	Quartz	6.1–19.3	0.96–1.02
ABLK-10	28	118–168	−14.9 to −4.4	5–10	4–10	Quartz	7.0–18.5	0.99–1.07
ABLK-11	18	127–195	−15.3 to −6.7	5–10	4–9	Quartz	10.1–18.9	0.95–1.03
ABLK-15	28	131–190	−14.5 to −4.9	5–10	4–10	Quartz	7.7–18.2	0.94–1.03
TM-19	72	105–218	−16.4 to −1.4	5–30	4–12	Dolomite	2.4–19.8	0.92–1.04
TM-7	12	125–149	−7.7 to −1.4	5–10	4–7	Dolomite	2.4–11.3	0.96–1.00
TM-20	13	118–193	−6.4 to −1.2	5–10	3–9	Dolomite	2.1–9.7	0.92–1.01
KLG-14	22	103–230	−17.1 to −5.3	5–10	4–9	Quartz	8.3–20.3	0.89–1.02
KLG-05	37	114–200	−16.2 to −6.2	5–10	3–13	Quartz	9.5–19.6	0.95–1.09
KLG-10	26	111–180	−19.4 to −4.9	5–10	4–10	Quartz	7.7–22.0	0.97–1.07

Explanations: TKLK—Tiekelike; ABLK—Abalieke; TM—Tamu; KLG—Kalangu. The samples separately collected from the main ore body.
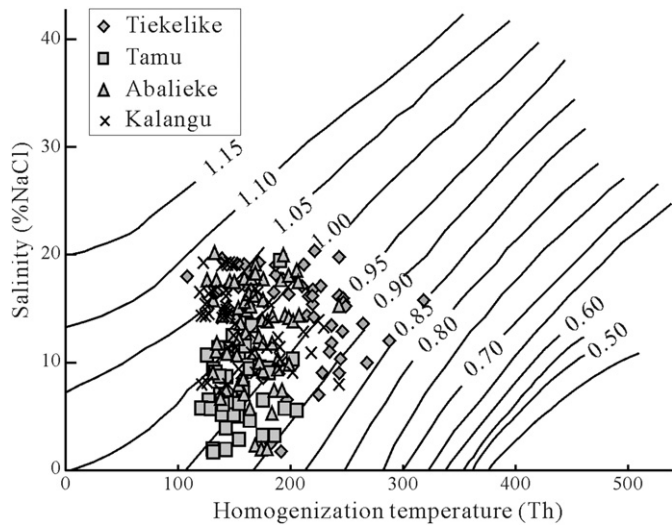
Fig. 16. Diagram showing the relationship between the temperature, salinity, and density of the fluid inclusions from the Tiekelike, Tamu, Abalieke, and Kalangu deposits (base map from Ahmad and Rose, 1980).

Due to the differences in the permeability between the breccia zones and the surrounding rock, the geothermal fluid moved into the breccia zones to form localized SEDEX systems (Fig. 18-B).

Ore-forming elements, such as the lead in the basement and the copper in the Devonian sandstone, became involved in the mineralization because the syndepositional faults cut through the basement. The extrusive facies are mainly stratiform or stratoid forms disseminated within specific strata. The conduit facies occur mostly as veins and breccia agglomerates in the breccia zones, while the ores mostly occur in fine-veined or disseminated massive forms.

The transformational mineralization occurred between the end of the late Paleozoic and the Triassic period. Coinciding with the regional orogenic uplift stage during the Triassic period (Fig. 18-C), the lateral extension of the orogenic belt resulted in faulting and the formation of an intermountain basin, while the vertical extrusion formed a fold. Consequently, the original distribution of the deposited sulfides was modified, and the ore adopted a different morphology in the fold zones. In addition, the tectonic stress was mostly centered axially and tended to produce interlayer fractures, providing void space for the ore-bearing hydrothermal fluid. When the horizontal tensional fault was above the fold near the axial portion, a preferred environment formed with a local temperature/pressure change and a contribution from meteoric water. Consequently, the metal component in the transformational hydrothermal fluid precipitated to form ore bodies that generally exhibited fine veined and networked textures (similar to the mineralization of orogenic deposits, Chen et al., 2000; Chen et al., 2012a; Chen et al., 2012b; Zhang et al., 2012; Zheng et al., 2013a; Zheng et al., 2013b). The post-depositional vein ore body overlaid the early stage stratiform

Fig. 17. Diagram showing the order of the metallogenic phase and mineral formation in the Tiekelike, Tamu, Abalieke, and Kalangu deposits.
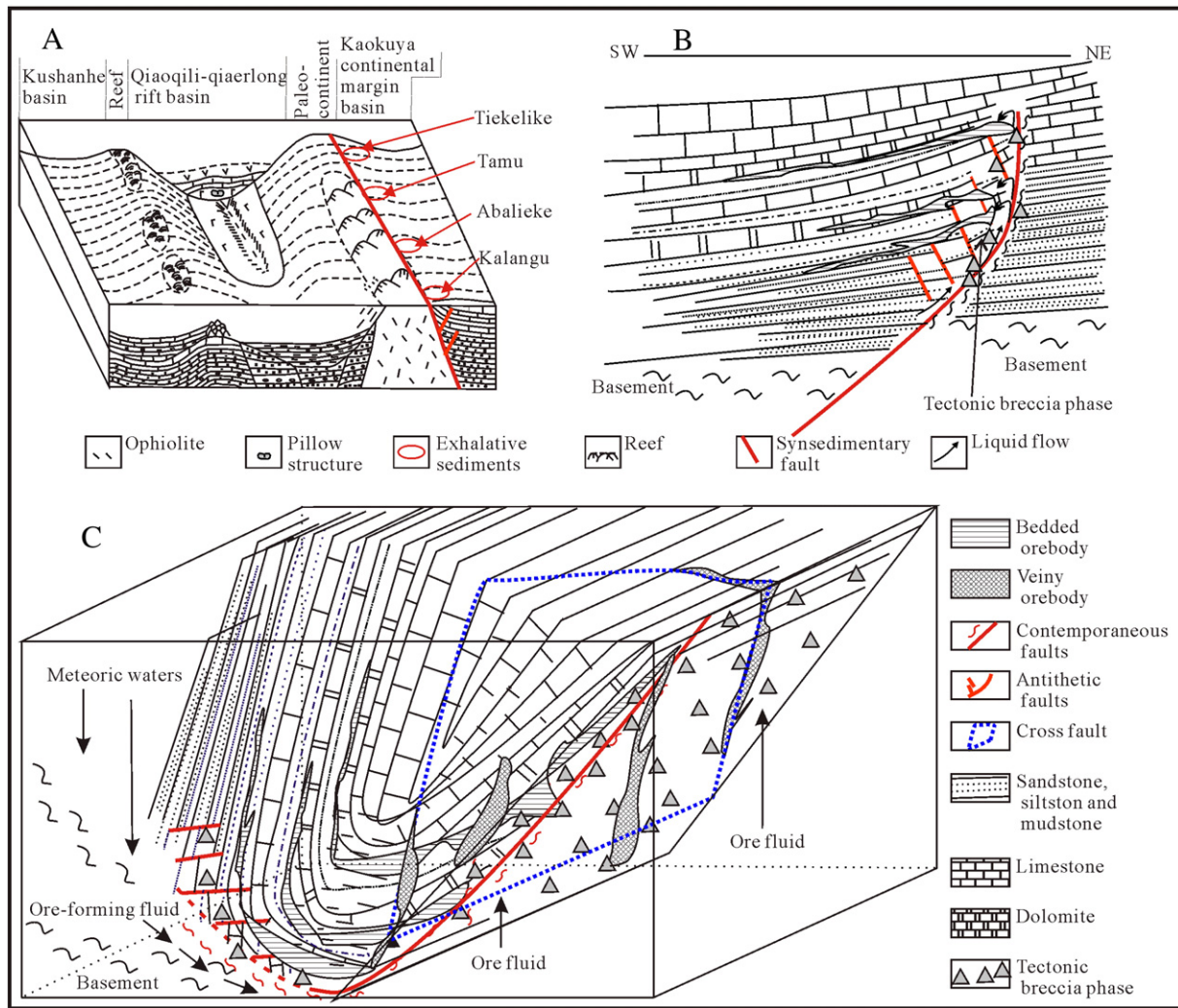
Fig. 18. Diagram showing the metallogenic model of the syndeposition and epigenetic modification. (A) Late Devonian–Carboniferous, continental margin sedimentary basin and synsedimentary fault. (B) Section of the tectonic breccia phase composed of contemporaneous faults and antithetic faults. (C) Triassic orogenic process, deformational metallogenic model.

ore bodies in the intersection zone between the fault and the breccia zone.

6. Conclusions

The host rocks of the Pb–Zn–Cu deposit in western Kunlun consist mostly of magnesium carbonate formed at the concavity basin along the margin of the Tarim Platform coincident with the initial Paleo-Tethys expansion during the late Paleozoic era. The Paleo basin has undergone several tectonic events associated with the Paleo-Tethys expansion, Paleo-Tethys closure, and post-Triassic orogeny, resulting in multiple stages of mineralization. Based on recent field observations, as well as laboratory-based geochemical and isotopic analyses, we concluded that the Pb–Zn–Cu deposits in western Kunlun were formed by syn-deposition (from 331 to 337 Ma) and post-depositional (from 206 to 235 Ma) mineralization.

Due to the multi-stage mineralization processes, the deposits are located in areas where the faults are superimposed on the cores of the fold structures. During the faulting events, the pressure gradient likely resulted in ore-bearing fluids being focussed toward open voids within the folds and fault structures. Changes in the physical and chemical conditions in these areas would trigger the precipitation of ore-forming elements from the mineralization fluid, forming deformational (or orogenic) deposits.

References

Ahmad, S.N., Rose, A.W., 1980. Fluid inclusions in porphyry and skarn ore at Santa Tita, New Mexico. Econ. Geol. 75, 229–250.

Anderson, G.M., 1975. Precipitation of Mississippi Valley-type ores. Econ. Geol. 70, 937–942.

Belyaevsky, N.A., 1949. The main features of the stratigraphy of western Kunlun. Izv. Akad. Nauk. SSSR Ser. Geogr. 2, 19–30 (in Russian).

Bi, H., Wang, Z.G., Wang, Y.L., Zhu, X.Q., 1999. History of tectonic–magmatic evolution in the western Kunlun orogeny. Sci. China D 29, 398–406 (in Chinese).

Brown, J.S., Maryland, T., 1970. Mississippi valley type lead–zinc ores: a review and sequel to the "Behre symposium". Miner. Deposita 5, 103–119.

Cannon, R.S., Pierce, J.A.P., Dekevaux, M.H., 1963. Lead isotope variation with growth zoning in a galena crystal. Science 142, 574–576.

Chang, X.S., 2003. Metallogenic characteristics and prospects of lead–zinc deposit in the western Kunlun. Xinjiang Nonferrous Metall. 26, 2–4 (in Chinese).

Chen, Y.J., Chen, H.Y., Liu, Y.L., Guo, G.J., Lai, Y., Qin, S., et al., 2000. Progress and records in the study of endogenetic mineralization during collisional orogenesis. Chin. Sci. Bull. 45 (1), 1–10.

Chen, S.J., Li, R.S., Ji, W.H., Zhao, Z.M., Liu, R.L., Jia, B.H., et al., 2010. The Permian lithofacies paleogeographic characteristics and basin–mountain conversion in the Kunlun orogenic belt. Geol. China 37, 374–393 (in Chinese with English abstract).

Chen, H.Y., Chen, Y.J., Baker, M., 2012a. Evolution of ore-forming fluids in the Sawayaerdun gold deposit in the Southwestern Chinese Tianshan metallogenic belt. Northwest China J. Asian Earth Sci. 49, 131–144.

Chen, H.Y., Chen, Y.J., Baker, M., 2012b. Isotopic geochemistry of the Sawayaerdun orogenic-type gold deposit, Tianshan, northwest China: implications for ore genesis and mineral exploration. Chem. Geol. 310, 1–11.

Cheng, S.D., Xu, X., 2001. Tectonics map compiled with Xinjiang and neighbouring areas. Xinjiang Geol. 19, 33–37 (in Chinese with English abstract).

Cheng, S.D., Zhang, X.J., 2000. Geotectonic division of Xinjiang. Xinjiang Geol. 18, 293–296 (in Chinese with English abstract).

Cheng, S.D., Li, Y.Z., Wang, Y.L., 1993. Metallogenic characteristics and distribution pattern of mineral resources in Xinjiang. Miner. Depos. 12, 1–9 (in Chinese with English abstract).

Cui, J.T., Bian, X.W., Wang, G.B., 2006. Geological compositions and evolutions in western Kunlun Mountains. Geol. Shaanxi 24, 1–11 (in Chinese with English abstract).

Dong, L.H., Zhuang, D.Z., Feng, J., Zhang, L.C., 2007. The stratabound lead–zinc deposits of Xinjiang. Xinjiang Geol. 25, 339–344 (in Chinese with English abstract).

Feng, G.Y., Liu, S., Peng, J.T., Zhang, Z.W., Qi, H.W., Zhu, X.Q., et al., 2009. Characteristics of fluid inclusions from Tamu-Kalangu lead–zinc metallogenic belt, Xinjiang. J. Jilin Univ. (Earth Sci. Ed.) 39, 406–414 (in Chinese with English abstract).

Henan Institute of the Geological Survey, 2006. Geological Map of the P.R.C. (1:250000 Scale Geological Map in Yingjisha County). J43 C 002003. p. 1 (in Chinese).

Heyl, A.V., Delevaux, M.H., Zartman, R.E., Brock, M.R., 1966. Isotopic study of galenas from the upper Mississippi Valley, the Illinois–Kentucky, and some Appalachian Valley mineral districts. Econ. Geol. 61, 933–961.

Hou, M.T., Gao, J., Jin, P., Liu, A., Li, X.L., 2007. The discovery of Kuerliang basic magmatic belt in northern Kunlun Mountains and its significance for mineral prospecting. Xinjiang Geol. 25, 18–25 (in Chinese with English abstract).

Ji, W.H., 2005. The Late Paleozoic Early-Mesozoic Tectonic Frame in the Western Kunlun–Karakorum area. China University of Geosciences for Doctoral Degree, Beijing pp. 1–143 (in Chinese with English abstract).

Jia, Q.Z., Li, W.M., Yu, P.S., Wu, J.R., Zhang, D.S., Gao, P., et al., 1999. Massive Sulfide Copper Deposits of West Kunlun. Xinjiang. Geological Publishing House, Beijing pp. 1–130 (in Chinese).

Jiang, C.F., Yang, J.S., Feng, B.G., 1992. The expand–close geotectonics in Kunlun Mountains. Geology Publishing House, Beijing pp. 1–136 (in Chinese).

Koppers, A.A.P., 2002. Ar–Ar CALC-software for $^{40}Ar/^{39}Ar$ age calculations. Comput. Geosci. 28, 605–619.

Kuang, W.L., Liu, G.S., Zhu, Z.Q., Liu, S.H., 2002. Metallogenesis of Kalangu MVT lead–zinc deposits and sources of minerogenetic materials in western Kunlun. Geotecton. Metallog. 26, 423–428 (in Chinese with English abstract).

Leach, D.L., Sangster, D.F., Kelley, K.D., Large, R.R., Garven, G., Allen, C.R., et al., 2005. Sediment-hosted lead–zinc deposit: a global perspective. Econ. Geol. 100, 561–607.

Li, Z.X., Yin, F.G., 2002. Comparative study of the geological structure of the east–west Kunlun Mountains. Geol. Bull. China 21, 777–783 (in Chinese with English abstract).

Li, G., Qi, W.X., Lu, J.G., 2007. Geological characteristics and the genetic type of Au–Fe–Cu deposit at the kua, west Kunlun Mountain. Xinjiang Geol. 25, 49–53 (in Chinese with English abstract).

Liu, X., 2001. Sedimentary-tectonic evolutionary history of the Tianshan to West Kunlun area in West China. J. Palaeogeogr. 3, 21–31 (in Chinese with English abstract).

Liu, Z.R., Xi, B.X., Yuan, W.X., Liu, C.R., 2003. Sedimentary facies and characteristics of Carboniferous and Permian of Southwest margin of Qimugen-Sangzhuhe district in Tarim basin. Xinjiang Geol. 21, 280–285 (in Chinese with English abstract).

Lu, Y.F., 2004. GeoKit—a geochemical toolkit for Microsoft Excel. Geochemical 33, 459–464.

Ludwig, K.R., 1994. Isoplot—a plotting and regression program for radiogenic-isotope date. US Geol Surv Open-file Report, Version 2.75 pp. 91–445.

Mattem, F., Schneider, W., Li, Y., Li, X., 1996. A traverse through the western Kunlun (Xinjiang, China): tentative geodynamic implications for the Paleozoic and Mesozoic. Geol. Rundsch. 85, 705–722.

Nakai, S., Halliday, A.N., Kesler, S.E., Jones, H.D., 1990. Rb–Sr dating of sphalerite from Tennessee and the genesis of Mississippi Valley-type ore deposits. Nature 346, 354–357.

Nakai, S., Halliday, A.N., Kesler, S.E., Jones, H.D., Kyle, J.R., Lane, T.E., 1993. Rb–Sr dating of sphalerites from Mississippi Valley-type (MVT) ore deposits. Geochim. Cosmochim. Acta 57, 417–421.

Pan, Y.S., 1990. Tectonic feature and evolution of the western Kunlun Mountains. Sci. Geol. Sin. 25, 224–232 (in Chinese with English abstract).

Pan, Y.S., Wen, S.X., Sun, D.L., 2000. Geographical Evolution of Kala Kunlun Mountain–Kunlun Mountain. Science Publishing House, Beijing pp. 1–138 (in Chinese).

Qi, W., Hou, M.T., Gao, J., Jin, P., Cai, F.L., 2005. Geological characteristics and exploration prospecting of sulfide deposits of copper(nickel) in the northern Kunlun. Northwest. Geol. 38, 32–44 (in Chinese with English abstract).

Qi, L., Zhou, M.F., Wang, C.Y., Sun, M., 2007. Evaluation of a technique for determining Re and PGEs in geological samples by ICP-MS coupled with a modified Carius tube digestion. Geochem. J. 41, 407–414.

Qu, G.S., Li, Y.G., Zhang, N., Li, Y.F., Chen, J., Chen, X.N., et al., 2004. A study on the foreland structure of the Qimugen arc in southwest Tarim and its genetic mechanism. Geol. Rev. 50, 567–576 (in Chinese with English abstract).

Shen, N.P., You, F.H., Zhang, Z.W., Peng, J.T., Zhu, X.Q., Xiao, J.F., 2012. Geochemistry characteristics of lead isotope for the Pb–Zn–Cu deposits in the southwestern margin of Tarim, and its significance. Chin. J. Geochem. 31, 381–392.

Sun, H.T., Li, C.J., Wu, H., Wang, H.J., Qi, S.J., Chen, G.M., et al., 2003. The Metal Ore Deposit in West Kunlun Mountains. Geology Publishing House, Beijing pp. 1–255 (in Chinese).

Tian, P.R., Hu, Q.W., 2010. Regional metallogenic characteristics of Pb–Zn(Cu) ore deposit belt of late-Paleozoic arc marine hydrothermal-volcanic hydrothermal sedimentary type in the west Tarim. Miner. Explor. 1, 131–140 (in Chinese with English abstract).

Tu, G.C., 1984. Geochemistry of Stratabound Ore Deposits in China (Volume1). Science Press, Beijing pp. 1–354 (in Chinese).

Wang, Y.Z., Wu, Z.Z., 1997. Plate tectonic attribute in western Tarim basin. Xinjiang Petrol. Geol. 18, 7–12 (in Chinese).

Wang, Y.Z., Wu, Y.Z., Deng, L.D., 1985. The Instruction to the Geologic and Mineral Deposits Map of West–South Xinjiang (1:500,000). Xiiang Geological and Mineral Bureau, Urumchi p. 1 (in Chinese).

Wang, S.L., Wang, D.B., Zhu, X.Y., 2001. The fluid inclusion in MVT lead–zinc deposit in southwest margin of Tarim. Mineral Resour. Geol. 15, 238–242 (in Chinese with English abstract).

Wang, J.C., Cui, J.T., Luo, Q.Z., Bian, X.W., Zhu, H.P., Yang, K.J., Peng, H.L., Zhang, H.P., Wang, F., Lin, S.Y., Ge, S.M., Ma, Z.K., 2006. The discovery and tectonic significance of a small branch ocean basin in monggubao–pushouyuan, Tethys ocean of northern Kangxiwa, west Kunlun mountains. Geol. Shaaxi 24, 41–50 (in Chinese with English abstract).

Wang, H., Liu, J.P., Li, S.H., Chen, G.W., Ren, G.L., Zhao, L., 2008. Discovery of the porphyry molybdenum deposit from Kayizi in west Kunlun and its prospecting implication. Geotecton. Metallog. 32, 179–184 (in Chinese with English abstract).

Wolf, K.H., 1976. Handbook of Strata-Bound and Stratiform Ore Deposits. Elsevier Science Publishers, Amsterdam–Oxford, New York-Tokyo pp. 1–146.

Xiao, W.J., Windley, B.F., Liu, D.Y., Jian, P., Liu, C.Z., Yuan, C., et al., 2005. Accretionary tectonics of the western Kunlun orogeny, China: a Paleozoic–Early Mesozoic, long-lived active continental margin with implications for the growth of southern Eurasia. J. Geol. 113 (6), 687–705.

Xinjiang Geological and Mineral Bureau, 2003. Xinjiang Regional Geological Records. Geology Publishing House, Beijing pp. 491–493 (in Chinese).

Yang, K.M., 1994. The formation and evolution of the continental margin in western Kunlun. Geol. Rev. 40, 9–18 (in Chinese with English abstract).

Yang, X.R., 2009. Characteristics and genesis of Tamu Zinc–Lead ore deposit, Southwest Margin of Tarim. Chinese Academy of Sciences and Graduate University of Chinese Academy of Sciences, Beijing, China, Doctorate degree paper pp. 1–128 (in Chinese with English abstract).

You, F.H., Zhang, Z.W., Shen, N.P., Peng, J.T., Zhu, X.Q., Xiao, J.F., 2011. Sulfur isotope characteristics and its significance for lead–zinc ore belt in the southwestern margin of Tarim, Xinjiang. Bull. Mineral. Petrol. Geochem. 30, 449–457 (in Chinese with English abstract).

You, F.H., Zhang, Z.W., Shen, N.P., Zhang, Z.S., Zhou, L.J., Zou, X.Q., et al., 2012. Texture and structure characteristics of ore from typical deposits of lead–zinc ore belt in the southwestern margin of Tarim. Acta Mineral. Sin. 32, 041–051 (in Chinese with English abstract).

Yuan, B., 2007. Study of geological characteristics and enrichment regularities of mineralization of Kalangu, Tamu lead–zinc deposits, west Kunlun, Xinjiang province. Master's degree paper Jilin University, Changchun pp. 1–84 (in Chinese with English abstract).

Zartman, R.E., Doe, B.R., 1981. Plumbotectonics—the model. Tectonophysics 75, 135–162.

Zhang, Z.W., Peng, J.T., Zhu, X.Q., Xiao, J.F., Liu, S., Qi, H.W., et al., 2009. Regional metallotectonics of the lead–zinc deposits zone in southwestern margin of the Tarim plate. Bull. Mineral. Petrol. Geochem. 28, 318–329 (in Chinese with English abstract).

Zhang, Z.W., Peng, J.T., Shen, N.P., Zhu, X.Q., Xiao, J.F., Liu, S., et al., 2011a. Metallogenic Model and Prospecting for the Strata-Bound and Succeeding Transformation Lead–Zinc Deposits within Carbonate in the west Kunlun, China. China Science and Technology University Press, Hefei pp. 1–208 (in Chinese).

Zhang, Z.W., Qi, L., Shen, N.P., You, F.H., Zhang, Z.S., Zhou, L.J., 2011b. Re–Os isotopic dating of chalcopyrite from copper–lead deposit in Abalieke, west Kunlun, China. Acta Petrol. Sin. 27, 3123–3128 (in Chinese with English abstract).

Zhang, L., Zheng, Y., Chen, Y.J., 2012. Ore geology and fluid inclusion geochemistry of the Tiemurt Pb–Zn–Cu deposit, Altay, Xinjiang, China: a case study of orogenic-type Pb–Zn systems. J. Asian Earth Sci. 49, 69–79.

Zheng, Y., Zhang, L., Chen, Y.j, Pete, H., Chen, H.Y., 2013a. Metamorphosed Pb–Zn–(Ag) ores of the Keketale VMS deposit, NW China: evidence from ore textures, fluid inclusions, geochronology and pyrite compositions. Ore Geol. Rev. 54, 167–180.

Zheng, Y., Zhang, L., Guo, Z.L., 2013b. Zircon LA-ICP-MS U–Pb and biotite Ar-40/Ar-39 geochronology of the Tiemuert Pb–Zn–Cu deposit, Xinjiang: Implications for ore genesis. Acta Petrol. Sin. 29 (1), 191–204 (in chinese with English abstract).

Zhu, X.Y., Wang, D.B., Wang, S.L., 1998. Geology and sulfur isotope geochemistry of the Tamu–Kalangu lead–zinc deposits, Akto county, Xinjiang. Miner. Depos. 17, 204–214 (in Chinese with English abstract).